New CNES-CLS09 global mean dynamic topography computed from the combination of GRACE data, altimetry, and in situ measurements

M. H. Rio,[1] S. Guinehut,[1] and G. Larnicol[1]

Received 6 July 2010; revised 25 February 2011; accepted 12 April 2011; published 22 July 2011.

[1] An accurate knowledge of the ocean mean dynamic topography (MDT) is mandatory for the optimal use of altimetric data, including their assimilation into operational ocean forecasting systems. A new global 1/4° resolution MDT was computed for the 1993–1999 time period with improved data and methodology compared to the previous RIO05 MDT field. First, a large-scale MDT is obtained from the CLS01 altimetric Mean Sea Surface and a recent geoid model computed from 4.5 years of GRACE (Gravity Recovery and Climate Experiment) data. Altimetric sea level anomalies and in situ measurements are then combined to compute synthetic estimates of the MDT and the corresponding mean currents. While the RIO05 MDT was based on 10 years of in situ dynamic heights and drifting buoy velocities, the new field benefits from an enlarged data set of in situ measurements ranging from 1993 to 2008 and includes all hydrological profiles from the Argo array. Moreover, the processing of the in situ data has been updated. A new Ekman model was developed to extract the geostrophic velocity component from the drifting buoy measurements. The handling of hydrologic measurements has also been revisited. Compared to the previous RIO05 solution, the new global MDT resolves much stronger gradients in western boundary currents, with mean velocities being doubled in some places. Moreover, in comparison to several other recent MDT estimates, we find that the new CNES-CLS09 MDT is in better agreement with independent in situ observations.

Citation: Rio, M. H., S. Guinehut, and G. Larnicol (2011), New CNES-CLS09 global mean dynamic topography computed from the combination of GRACE data, altimetry, and in situ measurements, *J. Geophys. Res.*, *116*, C07018, doi:10.1029/2010JC006505.

1. Introduction

[2] The Gravity Field and Steady-State Ocean Circulation (GOCE) satellite was successfully launched in March 2009. As the first Earth Explorer core mission from the ESA Living Planet program, it will provide by the end of its 20 months lifetime an estimate of the geoid's scales down to 100 km with centimetric accuracy [*European Space Agency*, 1999]. After the huge success of the Gravity Recovery and Climate Experiment (GRACE) mission [*Tapley et al.*, 2003], this represents another important milestone for the measurement of the Earth's gravity field. Among the main beneficiaries of these successive improvements is the oceanographic community working with altimetric data. The geoid height N is indeed the missing quantity needed to compute (equation (1)) the ocean absolute dynamic topography (the sea level h above the geoid) from the altimetric measurement (the sea level η above a reference ellipsoid). Under the geostrophic assumption, ocean surface currents can then be derived from the absolute dynamic topography values

$$h = \eta - N. \quad (1)$$

[3] In practice, the absolute dynamic topography cannot be computed as the simple difference between the altimetric measurement and the geoid height, as this would require the knowledge of the geoid with centimetric accuracy at scales down to a few hundred meters. An altimeter provides one sea level height measurement roughly every 350 m along track, which are commonly averaged in order to reduce noise (standard along-track AVISO products for instance contains one measurement every 7 km). Alternatively, Sea Level Anomalies $h'_p = \eta'_p$ relative to a given time period P are computed using the repeat-track method [*Cheney et al.*, 1983], in which along-track mean altimetric profiles $\langle\eta\rangle_P$ are subtracted from the instantaneous altimetric heights η. To reconstruct the full dynamical signal h from the altimetric anomaly h'_p, an accurate estimate of the ocean mean dynamic topography (MDT) for the time period P is needed. The most straightforward approach (hereinafter called the "direct

[1]CLS, DOS, Ramonville Saint-Agne, France.

0148-0227/11/2010JC006505

method") is to subtract a geoid model from an altimetric Mean Sea Surface (MSS) defined as the gridded mean profiles $\langle \eta \rangle_P$, after making sure that both surfaces are consistent, and notably that they are expressed relative to the same ellipsoid and tide system (all details are given by *Hughes and Bingham* [2008]). However, an altimetric MSS resolves much shorter spatial scales (down to 10–20 km) than recent satellite-only (i.e., computed from space gravity data only) geoid models and, in order to match the spectral content of both surfaces, some form of filtering is needed. This can be done using simple filters such as Gaussian or Hamming [*Tapley et al.*, 2003; *Jayne*, 2006; *Bingham et al.*, 2008]. In order to remove as much noise as possible while minimizing signal attenuation, more complex filters may be used. For example, *Vianna et al.* [2007] and *Vianna and Menezes* [2010] developed an adaptive filter, based on principal components analysis techniques, while *Bingham* [2010] applied a nonlinear anisotropic diffusive filtering method. Whatever the filter used, the spectral content of the latest satellite-only geoid models based on GRACE data still limits the spatial resolution of the MDT computed through the direct method to scales larger than 200–300 km [*Rio*, 2010]. In order to estimate the MDT scales shorter than 200–300 km, different methods have been developed in the past few years.

[4] A first way to proceed is to improve the geoid resolution. This can be done using in situ gravimetric data [*Hunegnaw et al.*, 2009; *Thompson et al.*, 2009]. As in situ gravimetric data are limited in spatial extension, only regional improvements of the geoid are obtained. Global improvement can be achieved though using the shortest scales information of the altimetric MSS (the smallest spatial scales of the MDT being larger than those of the MSS, the smallest spatial scales of the altimetric MSS are only due to the smallest spatial scales of the geoid and can therefore be used to enhance the geoid). This method is commonly used to enhance the resolution of the satellite-only geoid models, resulting in the so-called "combined" geoid models which are developed to a higher degree and order than their satellite-only counterpart. In the case of the recent EGM08 earth gravity model [*Pavlis et al.*, 2008], both in situ gravimetric data and altimetry-derived gravity anomalies have been used to compute the spherical harmonic coefficients of the gravity field up to degree and order 2400 (~8 km resolution). *Andersen and Knudsen* [2009] used this geoid model, together with the DNSC08 altimetric MSS to compute spatial scales of the MDT greater than 75 km. The EGM08 model was also used recently by *Vianna and Menezes* [2010] for MDT computation on a 0.1° resolution grid.

[5] A second approach developed to compute high-resolution MDT is to first compute a large-scale MDT using the direct method and further improve it by using external oceanographic data to resolve the shortest scales. This method was applied by *Maximenko and Niiler* [2005] and *Maximenko et al.* [2009] using drifting buoy velocities, as well as by *Rio and Hernandez* [2004] and *Rio et al.* [2005, 2007] using both hydrological profiles and drifter velocities.

[6] Finally, the computation of high-resolution MDTs can be achieved by synthesizing all oceanographic information available (in situ and space measurements of the ocean state) in a dynamically consistent way through inverse modeling [*LeGrand et al.*, 2003], or through data assimilation into ocean general circulation models [*Ferry et al.*, 2010]. In that case, model outputs are averaged to obtain an estimate of the MDT over the required period.

[7] These continuous improvements achieved in recent years for estimating the MDT have led to a growing number of scientific studies using absolute altimetric heights [e.g., *Fu*, 2006; *Qiu and Chen*, 2010; *Saraceno et al.*, 2009]. Also, a number of ocean current products have been produced [*Bonjean and Lagerloef*, 2002; *Larnicol et al.*, 2006; *Sudre and Morrow*, 2008] that are obtained as the sum of the geostrophic component from absolute altimetry and an estimate of the Ekman component. These surface currents can be used for a number of applications such as ocean model validation, support to offshore activities, search and rescue, and oil spill monitoring. Operational ocean forecasting systems have also greatly benefited from higher-resolution MDTs. In the framework of the Geoid and Ocean Circulation in the North Atlantic (GOCINA) project, the use of an improved MDT in three different European operational forecasting systems led to changes in transport across key sections between Scotland and Greenland of up to 10–20% for mass transport and of about 30% for heat transport, resulting in an increased agreement with in situ observations [*Knudsen et al.*, 2006].

[8] Despite the indisputable progress that has been made in recent years toward estimating the ocean's mean circulation, further improvements are still needed, both in term of resolution and accuracy, to fully exploit the altimetric data in oceanographic applications.

[9] In this paper, we describe the calculation of a new global 1/4° resolution MDT, the CNES-CLS09 MDT, and the associated mean geostrophic currents for the time period P = 1993–1999. The approach is based on the three steps methodology used by *Rio and Hernandez* [2004] and *Rio et al.* [2005]. Compared to the MDT computed by *Rio et al.* [2005], hereinafter called the RIO05 MDT, a number of improvements have been made with the aim of providing, in preparation for the exploitation of GOCE data, a combined MDT based on updated data sets (as described in section 2) and methodology.

[10] The first step of the method is to compute a large-scale estimate of the MDT (the so-called first guess) by filtering the difference between an altimetric MSS and a geoid model. A filtering technique based on optimal interpolation has been developed (section 3), which is much more efficient compared to the classical Gaussian spatial filtering applied by *Rio and Hernandez* [2004] and *Rio et al.* [2005]. Next, synthetic estimates of the MDT $\langle h \rangle$ and the associated mean geostrophic currents ($\langle u_g \rangle$, $\langle v_g \rangle$) are calculated. These are simply obtained, for a given time t and geographical position, by subtracting from the instantaneous in situ measurements of the ocean dynamic topography h(t) or the ocean geostrophic surface current $u_g(t)$,$v_g(t)$, the time variable ($h'_a(t)$, $u'_a(t)$, $v'_a(t)$) component as measured by altimetry:

$$\langle h \rangle = h(t) - h'_a(t) \qquad \langle u_g \rangle = u_g(t) - u'_a(t) \qquad \langle v_g \rangle = \langle v_g \rangle(t) - v'_a(t). \tag{2}$$

[11] Two different types of oceanographic in situ measurements are used in this study, surface velocities measured by drifting buoys and dynamic heights computed from in situ

hydrological profiles. To ensure consistency with the physical content of the altimetric height and velocity anomalies, the implementation of the synthetic method requires the preliminary processing of the in situ data as follows:

[12] 1. The proper modeling and removal from the raw drifting buoy velocities of the Ekman currents due to the ageostrophic response of the ocean to wind stress forcing is required. The Ekman model used for processing the drifting buoy velocities in the RIO05 MDT computation had been derived by *Rio and Hernandez* [2003]. A new model, fully described in section 4, has been developed for the present study.

[13] 2. The correction of the dynamic heights computed relative to a given reference depth (the depth of the T/S profile used) for the missing barotropic component and the deep baroclinic component (from the profile's depth to the bottom) is also required. For the RIO05 MDT computation, a single reference level of 1500 m was chosen for all hydrological profiles, limiting the number of data to areas with bathymetric depths greater than 1500 m. In this study, a methodology has been implemented to take into account the information from hydrological profiles whatever their reference depth (section 5). This allows us to include profiles taken in shallow waters and data from deeper profiles in our calculation.

[14] Finally, the synthetic estimates are used to improve the large-scale solution (both for mean heights and mean geostrophic velocities) from the direct method through a multivariate objective analysis (section 5.3). The final 1/4° global CNES-CLS09 MDT is validated against independent observations and other existing MDTs in section 6. Conclusions and perspectives are given in section 7.

2. Data

[15] The computation of the CNES-CLS09 MDT as described in this paper is based on a number of data sets: a geoid model (section 2.1), an altimetric Mean Sea Surface as well as altimetric Sea Level Anomalies (section 2.2), wind stress data (section 2.3), and oceanographic in situ data (section 2.4).

2.1. Geoid Model

[16] The gravity model used in this study is the satellite-only EIGEN-GRGS.RL02 static field computed at GRGS-GFZ by *Bruinsma et al.* [2010] using 4.5 years of GRACE data. It is defined until the degree/order 160 of a spherical harmonic expansion (corresponding to a spatial resolution of 125 km). The grid of geoid height is provided in the tide free system and relative to the GRIM ellipsoid. In order to be consistent with the CLS01 Mean Sea Surface, we have converted it to the mean tide system and the TOPEX ellipsoid.

2.2. Altimetric Data

[17] The altimetric data used in this study were computed at CLS in the framework of the SSALTO-DUACS project and are distributed by AVISO. Multimission, delayed mode, maps of Sea Level Anomalies are considered for the period ranging from January 1993 to July 2009. This time series is completed by real-time maps for the period ranging from July 2009 to July 2010. Both delayed-time and real-time multimission maps are available weekly on a 1/3° resolution grid following *Ducet et al.* [2000] and are referenced relative to the 1993–1999 mean time period. The altimetric Mean Sea Surface used in this study is the CLS01 solution, computed for the 1993–1999 time period by *Hernandez and Schaeffer* [2001]. Although more recent MSS solutions exist (for instance, the DNSC08 MSS computed by *Andersen and Knudsen* [2009]), the CLS01 MSS was used in order to base our work on a homogeneous data set of altimetric products, (i.e., SLA and MSS are based on altimetric data that have been processed using a consistent set of environmental, instrumental and geophysical corrections). Error maps for the altimetric anomalies and the MSS are also provided by AVISO.

2.3. Wind Stress Data

[18] Wind stress data are needed to estimate the Ekman currents as described in section 4. We have used 3-hourly, global, 80 km resolution wind stress maps from the ERA INTERIM reanalysis which is, as described by *Simmons et al.* [2006], an "interim" reanalysis of the period 1989 to present in preparation for the next-generation extended reanalysis that will replace the commonly known ERA-40 reanalysis.

2.4. Oceanographic in Situ Measurements

2.4.1. Drifting Buoy Velocities

[19] We have considered 15 m drogued drifting buoy data collected from 1993 to 2008 in the framework of the international Global Drifter Program. These data are distributed by AOML (Atlantic Oceanographic and Meteorological Laboratory), where they have first been quality controlled and krigged [*Hansen and Poulain*, 1996] in order to provide 6-hourly velocity measurements.

[20] Figure 1 shows the number of velocity measurements available by latitudinal bands and by basins from 1993 to 2008 and, in black, from 1993 to 2002 (previously used for the RIO05 MDT computation). In all basins, and at all latitudes, the number of data has greatly increased between 2002 and 2008, resulting in a much better sampling of the global ocean. Notably, the high latitudes are now much better sampled.

2.4.2. Hydrological Profiles

[21] Temperature and salinity profiles measured from the surface to varying depths by Argo floats (from 2002 to 2008) or conductivity-temperature-depth (CTD) casts (from 1993 to 2008) and distributed by the Coriolis Global Data Acquisition Center (http://www.coriolis.eu.org) are used in our analysis. The full Argo data was obtained in July 2009. The full data set has passed through the real-time quality control procedures applied by each Data Acquisition Center, and about half of the profiles older than one year have passed through delayed-mode procedures; see the Argo quality control manual for more details (A. P. S. Wong et al., Argo quality control manual, 2010, http://www.argodatamgt.org/content/download/341/2650/file/argo-quality-control-manual-V2.6.pdf.). For this study, when available, delayed-mode fields are preferred to real-time ones and only measurements having position, date, pressure, temperature and salinity observations considered "good" (i.e., with a quality flag numerical grade of "1") are used. Additional editing was performed in order to exclude floats showing discrepancies between dynamic height anomalies calculated from Argo with collo-

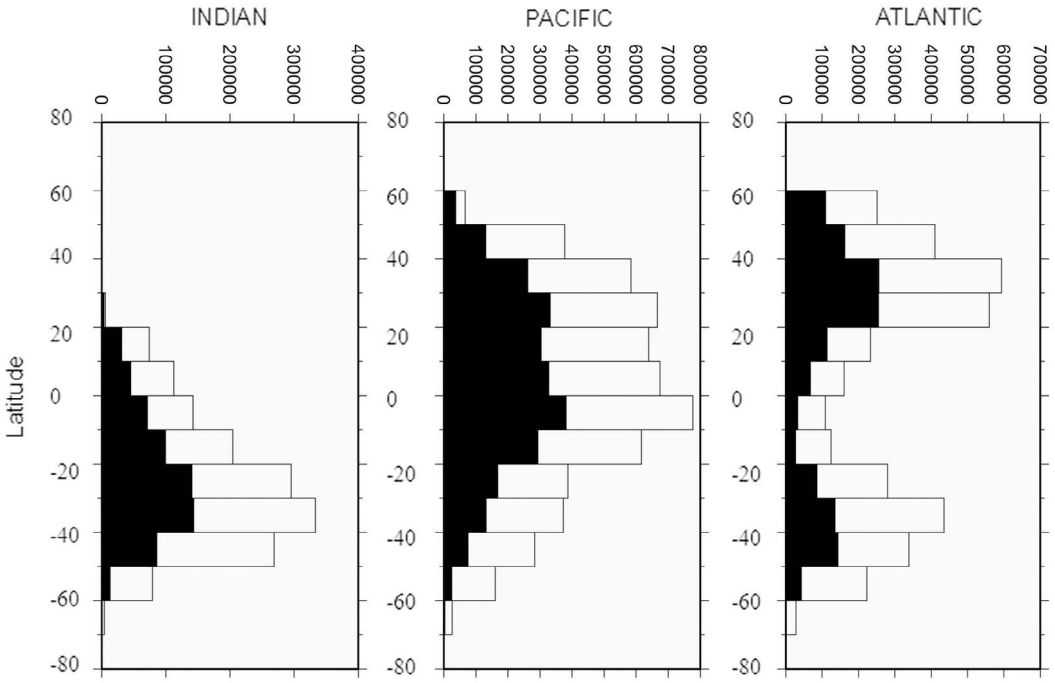

Figure 1. Number of drifting buoy velocities available from 1993 to 2008 (and in black from 1993 to 2002) by latitudinal band and by basin.

cated satellite altimetry observations following the method developed by *Guinehut et al.* [2009]. For example, the floats showing systematic pressure errors such as those detected by *Willis et al.* [2009] have been either corrected or excluded.

[22] Figures 2a and 2b show the maximum depths of the T/S profiles measured by the Argo floats and the CTD profiles, respectively. While the spatial coverage of the CTD profiles is sparse, with large regions unsampled, the deployment of the Argo array from 2002 to 2008 has allowed a much more complete horizontal spatial sampling of the oceans. On the vertical, the maximum Argo profiles depth is 2000 m although the majority of the profiles go down to 900 m only. In contrast, CTD profiles may sample the vertical structure of the ocean density down to 5000 m depth. The data sets are therefore to some extent complementary. In the RIO05 MDT computation only hydrological profiles prior to 2002 were considered.

3. Large-Scale First Guess Computation Through Optimal Filtering

[23] The simple difference between the CLS01 Altimetric MSS and the EIGEN-GRGS.RL02 static geoid model is shown in Figure 3a. As stated in section 2, the geoid model is defined until the degree/order 160 of a spherical harmonic expansion (125 km resolution). The resulting MDT (hereinafter called CLS01mEIGEN MDT) is therefore polluted by short-scale structures of the geoid that are resolved by the

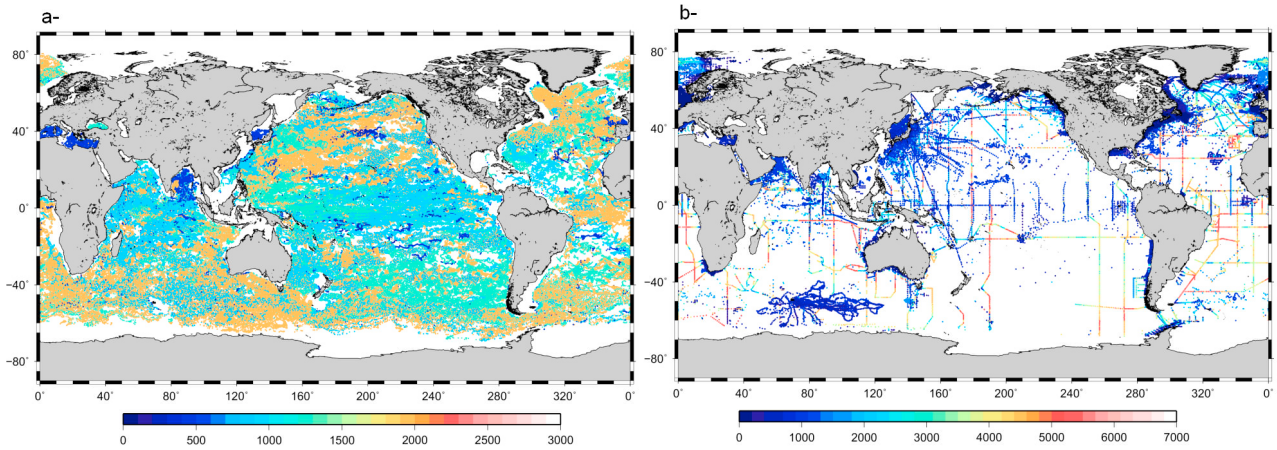

Figure 2. (a) Argo profiles from 2002 to 2008. (b) CTD profiles from 1993 to 2008. The color scale corresponds to the hydrological profile's depth.

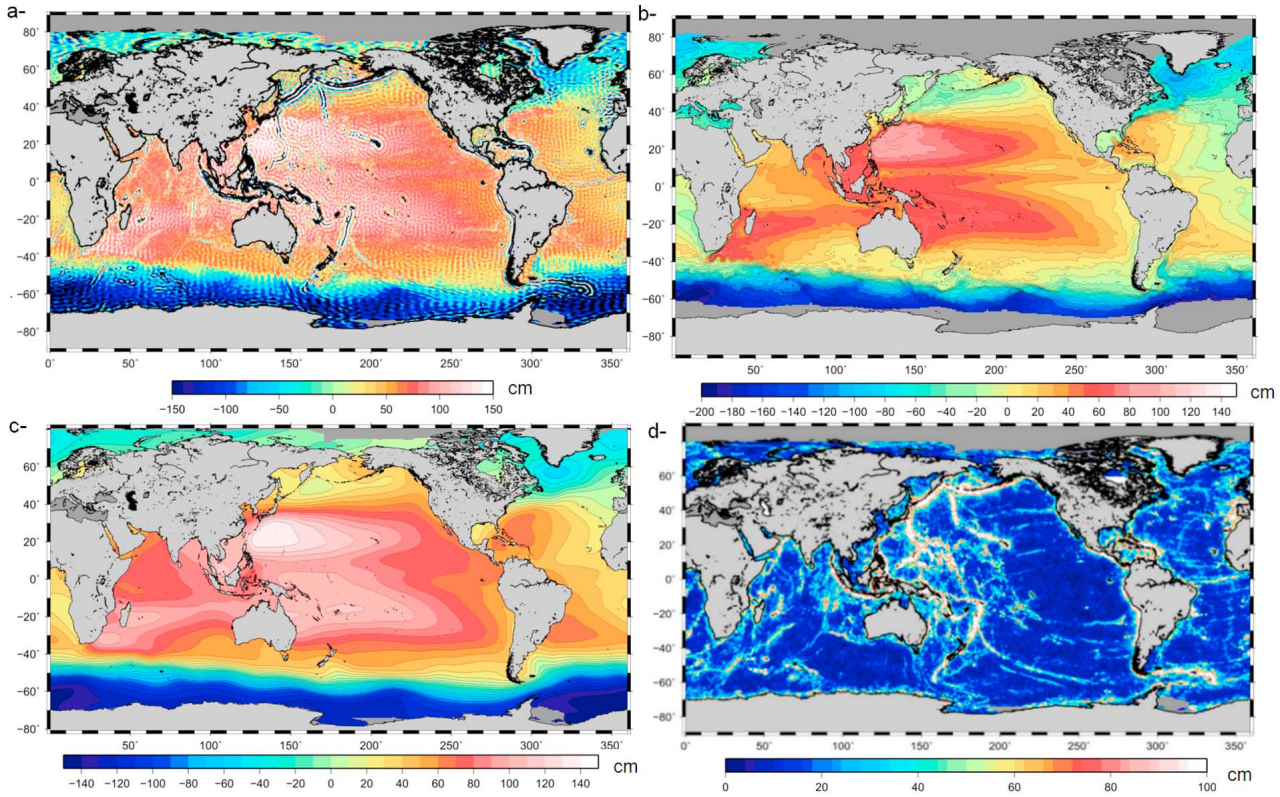

Figure 3. (a) MSS CLS01 minus EIGEN-GRGS.RL02 static geoid model. (b) The GLORYS1v1 MDT. (c) Associated MSS CLS01 minus EIGEN-GRGS.RL02 filtered to remove scales shorter than 1000 km. (d) Errors computed as the variance of the differences between the observations and the a priori MDT.

MSS but not by the EIGEN-GRGS.RLS02 geoid model. In addition, the truncation of the geoid model at the degree/order 160, projected in the spatial domain, generates Gibbs oscillations which radiate from regions of large topographic gradients [*Bingham et al.*, 2008]. Filtering is needed to remove this noise. Traditional spatial filters (such as the Gaussian filter) consist of a weighted average of observations surrounding the grid point where the filtered field is computed. The weights depend only on the distance between the observations and the grid point. The correct elimination of high-amplitude short-scale errors may result on the other hand in an overfiltering of realistic short-scale signals (sharp gradients in strong currents for instance). With the aim of resolving this issue, we have used an optimal filtering approach, where both the errors on the CLS01mEIGEN MDT and the a priori statistical characteristics of the MDT are taken into account, as described below.

3.1. Optimal Filtering Approach

[24] The raw differences between the CLS01 Altimetric MSS and the EIGEN-GRGS.RL02 static geoid model on a global grid (Figure 3a) are used as input observations to an objective analysis [*Rio and Hernandez*, 2004]. In this formulation, the optimally filtered MDT $\langle h \rangle(r)$ is obtained at the spatial position r as a linear combination of the raw observations $O(r_i)$:

$$\langle h \rangle(r) = \sum_{i=1}^{N} \alpha_i O(r_i) \text{ where } \alpha_i = \sum_{j=1}^{N} A_{i,j}^{-1} C_{r,j}, \qquad (3)$$

where A is the observations covariance matrix and $\vec{C}$ is the covariance vector between the observations and the estimated field. Under a number of hypotheses (homogeneity and isotropy), the covariance between two locations i and j only depends on the distance d_{ij} between the observations:

$$A = \left(\langle \sigma^2 \rangle C(d_{ij}) + \langle \varepsilon_i \varepsilon_j \rangle\right)_{i,j=1,N}, \quad \vec{C}_r = \left(\langle \sigma^2 \rangle C(d_{rj})\right)_{j=1,N},$$

where σ^2 is the a priori MDT variance, C(r) is the a priori correlation function of the MDT field, and ε_i is the error on the observation located at r_i. The error on the estimated field is then given by

$$\varepsilon(r) = \sigma^2 - \sum_{i=1}^{N} \sum_{j=1}^{N} A_{i,j}^{-1} C_{r,i} C_{r,j}. \qquad (4)$$

[25] As in the work of *Rio and Hernandez* [2004], we use the correlation function introduced by *Arhan and Colin de Verdiere* [1985], $C(r) = (1 + r + \frac{1}{6}r^2 - \frac{1}{6}r^3)e^{-r}$, where $r = \sqrt{\left(\frac{x}{x_0}\right)^2 + \left(\frac{y}{y_0}\right)^2}$ and x_0 and y_0 are the zonal and meridian correlation radii of the MDT (the values of which are obtained in section 3.3).

[26] In theory, the mean of the estimated field needs to be zero [*Bretherton et al.*, 1976]. In practice, this hypothesis is fulfilled by first removing from the observations a large-scale a priori solution which is added back to the estimated field after inversion. This large-scale a priori solution is obtained by smoothing the raw observations with a

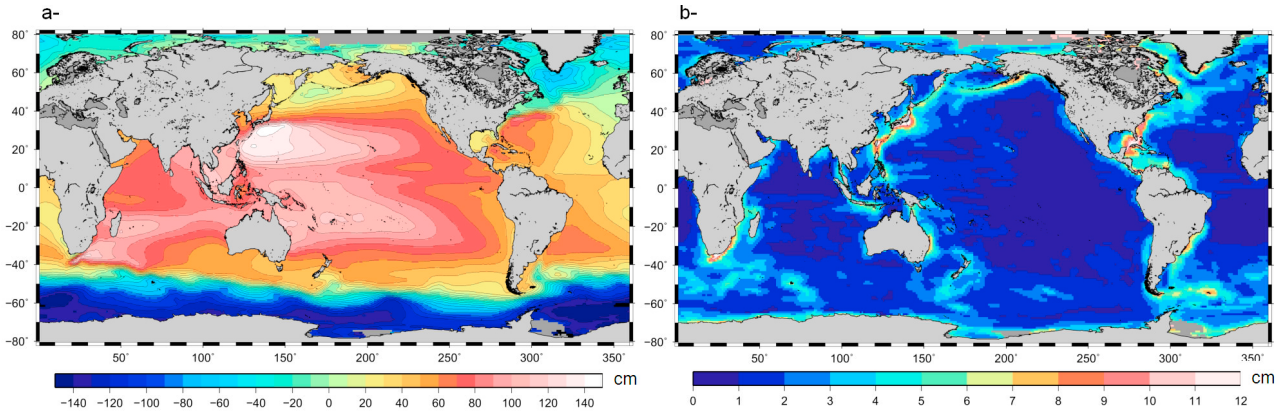

Figure 4. (a) Result of the optimal filtering applied on the raw MSS CLS01 minus EIGEN-GRGS.RL02 observations. (b) Estimated error field.

Gaussian low-pass filter to remove spatial scales shorter than 1000 km (Figure 3c).

[27] For each grid point where the optimally filtered field is computed, the weights on the surrounding observations therefore depend both on the distance to the grid point and on the observation error. The distance dependence is fully defined through the covariance field (variance and correlation radii) of the MDT. This method therefore requires the knowledge of both observation error and the a priori MDT covariance field.

3.2. Observation Errors

[28] Errors on the observations can be written as the quadratic sum of the formal errors on the MSS and the geoid. We obtain (not shown) a rather uniform error field with values ranging from 6 cm at high latitudes to 10 cm at low latitudes, governed by the geoid formal error. This, however, is an underestimate of the true error, since it does not take into account the omission error of the geoid (due to the geoid scales shorter than 125 km resolved by the MSS but not resolved by GRACE data). To have a full appreciation of the observation errors, we compare the CLS01mEIGEN MDT to an a priori estimate of the MDT (Figure 3b) computed at a 1/4° resolution in the framework of the Global Ocean ReanalYsiS (GLORYS) of the French Mercator operational forecasting system [*Ferry et al.*, 2010].

[29] Figure 3d shows the root-mean-square differences, computed in 1° boxes, between the GLORYS MDT and the CLS01mEIGEN MDT. Away from steep bathymetric gradients, values are lower than 20 cm. They increase up to more than 1 m along sharp geodetic structures (such as subduction zones or rifts). This, however, is an overestimate of the true error. Part of it is due to the variability, in 1° boxes, of the mean circulation as seen by the GLORYS field. We assess this contribution by computing the GLORYS MDT variance into 1° boxes and remove it from the estimated error field. Any error on the GLORYS MDT will also contribute to the computed root-mean-square (RMS) difference. These errors are due to errors in the Mercator model and are therefore very difficult to quantify, so that we might still overestimate slightly the error in our observations. Finally, we associate for each grid point of the CLS01mEIGEN MDT an observation error equal to the maximum value between the formal error and the error deduced from the comparison with the GLORYS MDT.

3.3. A Priori MDT Covariance

[30] We use the GLORYS MDT to estimate the a priori variance and correlation function of the MDT. As mentioned in section 3.1, the application of the objective analysis method requires zero-averaged observations, and we have consequently removed from the raw observations the spatial scales larger than 1000 km, in order to reduce the observations means. We therefore need to model the covariances of the MDT scales which are shorter than 1000 km. We remove from the GLORYS MDT the scales greater than 1000 km (applying the same Gaussian filter as before) and compute the variance and the correlation function on the residual field. The computed correlations are compared to the theoretical model C(r) from section 3.1 and the zonal and meridian correlation radii x_0 and y_0 are deduced by least square fit. The covariance matrix A needs to be well conditioned to be properly inversed. This requires a smooth correlation radii spatial field, which is obtained applying a 3000 km cutoff length Gaussian filter. Maximum values of zonal (meridian) correlation radius of 2000–3000 km (1500–2000 km) are obtained in the tropical band. Lower values (lower than 1000 km in zonal, 500 km in meridian) are obtained at midlatitudes and high latitudes as well as in coastal areas. We investigate the sensitivity of the correlation radii thus obtained to the a priori MDT by repeating the calculation using a different MDT, based on three years (1993–1995) of a 1/4° resolution OCCAM model run [*Fox and Haines*, 2003]. The OCCAM MDT was readjusted to the 1993–1999 time period. The values obtained are very close to the correlation radii computed from the GLORYS MDT, with only slightly higher values in the central tropical Pacific Ocean.

3.4. Results

[31] Figure 4a shows the large-scale MDT field obtained as an output of the objective analysis. The short scales of the residual geoid as well as the numerical Gibbs error arising from the truncation of the geoid have been removed by the optimal filter. Sharp gradients are visible in the Antarctic Circumpolar Current and the Western Boundary currents. Well known semipermanent structures of the ocean circu-

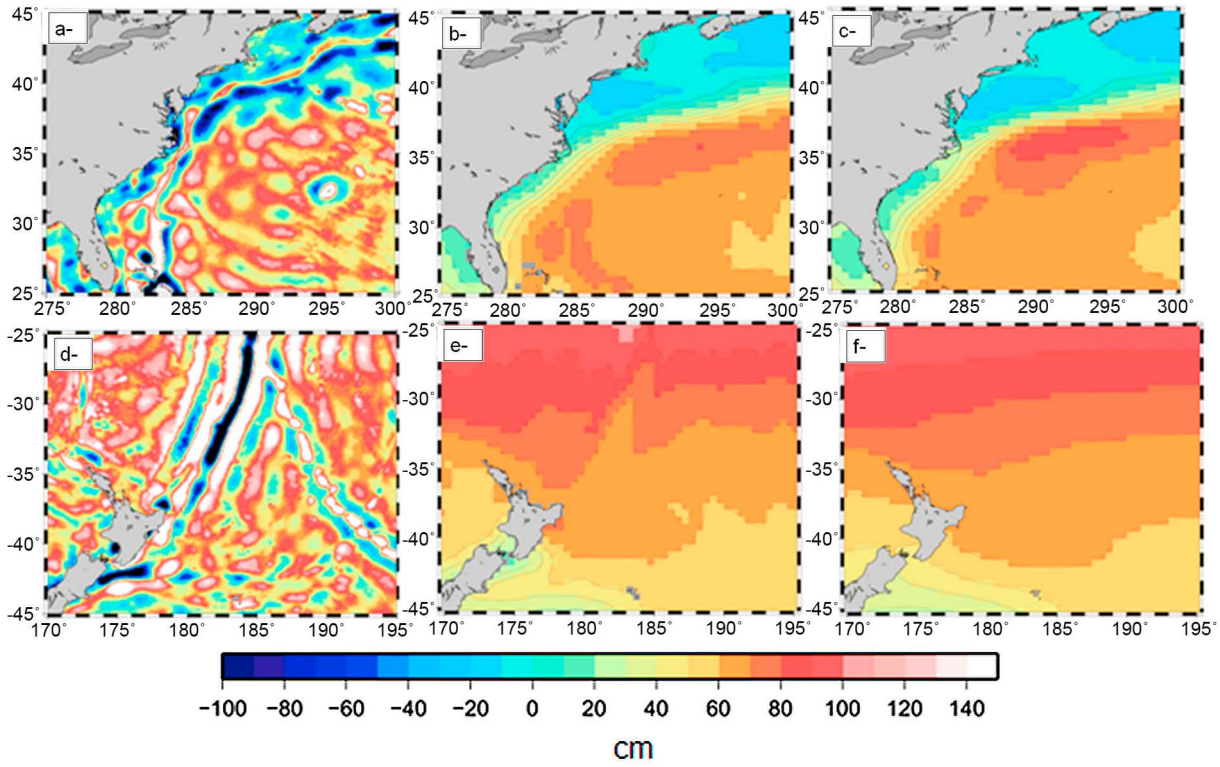

Figure 5. Comparison of Gaussian and optimal filter in (a–c) the Gulf Stream area and (d–f) the subduction zone northeast of New Zealand. Raw difference between the CLS01 MSS and the EIGEN-GRGS.RL02 geoid model (Figures 5a and 5d), MDT obtained applying a 400 km low-pass Gaussian filter (Figures 5b and 5e), and MDT obtained applying an optimal filter (Figures 5c and 5f).

lation are resolved (for example, the Mann Eddy at 40°N, 44°W in the Atlantic and the Zapiola anticyclone at 45°S, 43°W in the Atlantic). Following equation (4), an estimate of the error on the filtered field is also available as an output of the objective analysis (Figure 4b). Values of up to 10 cm are obtained in coastal areas or in strong boundary currents, while the error is less than 3–4 cm in the open ocean. Using the correlation radii computed from the OCCAM MDT makes very little difference to the final result. The root-mean-square difference between the two solutions is only 0.7 mm, with a mean difference of −0.2 mm. We are therefore confident that the final result does not depend significantly on the chosen a priori field used for the covariance matrix computation.

[32] The power of such an approach compared to the classical Gaussian filter is highlighted in Figures 5a–5c for the Gulf Stream region west of 300°E and in Figures 5d–5f for an area on the northeast of New Zealand. Figures 5a and 5d show the raw difference between the altimetric MSS and the geoid model. The signal is dominated by the short scales of the geoid resolved by the MSS but not by the geoid model. In subduction zones like the one located northeast of New Zealand, the resulting unfiltered MDT shows strong unrealistic gradients.

[33] If a 400 km cutoff length Gaussian filter is applied (Figures 5b and 5e), the noise in the Gulf Stream current is correctly removed but not in the New Zealand area, where an artifact in the MDT remains visible along the geodetic subduction zone. In order to remove this artifact, a higher cutoff length can be applied, but this also results in a further smoothing of the realistic Gulf Stream gradients (not shown). The use of the optimal filter (Figures 5c and 5f), which takes into account the observations errors (quite high along the New Zealand subduction zone), correctly smoothes the circulation in that area, while preserving (and even enhancing) the strong gradients of the Gulf Stream current.

[34] We have further checked the respective accuracy of the optimally filtered and the Gaussian filtered MDTs by using them to compute maps of absolute altimetric heights (adding them to the maps of Sea Level Anomalies described in section 2.2), and by derivation, weekly maps of absolute geostrophic velocities from January 1993 to December 2008. We have then interpolated the altimetric geostrophic velocities along the buoy trajectories available during this time period (described in section 2.4.1). Geostrophic velocities have been extracted from the drifting buoy velocities using the Ekman model described in section 4, and we have applied along the buoy trajectories, a 3 day low-pass filter. We computed the RMS differences and the vectorial correlation coefficient between the altimetric velocities and the geostrophic component of the buoy velocities. When the optimally filtered MDT is used to compute the absolute altimetric velocities, RMS differences to the geostrophic component of the drifting buoy velocities are reduced to 12.0 cm/s (11.4 cm/s) for the zonal (meridian) component of the velocity, compared to 12.9 cm/s (12.5 cm/s) obtained when the Gaussian filtered solution is used. Furthermore, the

vectorial correlation increases from 0.70 to 0.75. The values obtained for the Gulf Stream area and the New Zealand region from Figure 5 are consistent with the previous qualitative analysis; that is, in the Gulf Stream area the same statistical values are obtained whichever MDT is used to compute the absolute altimetric velocities. In contrast, in the New Zealand area, using the optimally filtered MDT reduces the RMS difference between the meridian components of the velocity (from 9.7 cm/s to 9.2 cm/s). Also, the vectorial correlation coefficient increases from 0.69 to 0.73. The large-scale MDT obtained by optimal filtering is statistically closer to observations than the Gaussian MDT and we will therefore use it later on in section 6 as a first guess for the estimation of the 1/4° resolution CNES-CLS09 MDT.

4. A New Ekman Model for Improved Synthetic Mean Velocities

4.1. Method

[35] To compute the synthetic mean velocities that will serve as input observations to the estimation of the CNES-CLS09 MDT, the time varying component of the geostrophic velocity as measured by altimetry is subtracted from the geostrophic component of the drifting buoy velocity (equation (2)). In the work of *Rio and Hernandez* [2004] and *Rio et al.* [2005], the extraction of the geostrophic component from the buoy velocity was done by first removing Ekman currents and then applying a 3 day low-pass filter to remove tidal and inertial currents as well as residual high-frequency ageostrophic signals. The Ekman model used was computed by *Rio and Hernandez* [2003] using a data set of drifting buoy velocities from 1993 to 1999 as well as the ECMWF wind stress analysis over the same period. In this model, the Ekman response of the ocean $\vec{u}_{ek}$ to the wind stress forcing $\vec{\tau}$ is written using a two-parameter (b, θ) formulation:

$$\vec{u}_{ek} = \frac{b}{\sqrt{f}}\vec{\tau}e^{i\theta} \tag{5}$$

with f being the Coriolis parameter.

[36] In this study, we use the data set of drifting buoys from 1993 to 2008 as well as the ERA INTERIM wind stress reanalysis to update the estimation of the b and θ parameters done by *Rio and Hernandez* [2003].

4.2. Results

[37] To estimate $\vec{u}_{ek}$ (equation (5)), absolute altimetric velocities computed from the AVISO altimetric SLA and the RIO05 MDT were interpolated along the drifting buoy trajectories available from 1993 to 2008 and subtracted from the buoy velocities. The residual ageostrophic current was further filtered using a 30 h to 20 day band-pass filter to focus on the frequencies where the coherency between the wind stress and the Ekman currents is at a maximum [*Rio and Hernandez*, 2003]. The ERA INTERIM wind stress values, interpolated along the drifting buoy trajectories were also band-pass-filtered. Then, the b and θ parameters were estimated by a least squares minimization. To be consistent with the *Rio and Hernandez* [2003] study, we first computed them for the whole time period, by season and in 5° by 5° boxes. Surprisingly, the updated parameters were found to differ significantly from the old ones, with higher b values and smaller $|\theta|$ values everywhere. To investigate further this important change, we repeated the b and θ estimation by latitudinal band and by year. b_{year} and θ_{year} obtained are displayed in Figures 6a and 6b, respectively. In all latitude bands, b_{year} is found to increase with increasing year while $|\theta_{year}|$ is found to decrease. We then removed this trend and repeated the minimization by months (using a 3 months sliding window) in order to capture the seasonal variability of the ocean Ekman response to the wind. The resulting b_{month} and θ_{month} are displayed in Figures 6c and 6d. Finally, we used the model given by equation (5) with $b = b_{year} + b_{month}$ and $\theta = \theta_{year} + \theta_{month}$ to remove the Ekman component from the drifting buoy velocities. Both the annual trend and the seasonal cycle of the newly computed parameters will be discussed in more detail in section 4.3.

[38] Figures 7a and 7b show, for the zonal and meridian components, respectively, the yearly root-mean-square difference between the altimetric absolute geostrophic velocities and the drifting buoy geostrophic velocities obtained using, either the Ekman model by *Rio and Hernandez* [2003] or the new Ekman model computed in this section. Before 1999, results are similar whichever Ekman model is used. After 2000 however, significantly reduced RMS differences are obtained for both components of the velocity using the new model. As we have seen previously, the Ekman response to wind stress as seen by 15 m drogue drifting buoys has changed over the last 15 years, so that the model fitted for the 1993–1999 period by *Rio and Hernandez* [2003] is no longer optimal for the data from more recent years. For both components of the velocity, we also observe an increase of the RMS difference from 1993 to 2008, which is linked to the increase in the buoy variability over the period: The zonal (meridian) velocity variability has increased from 16 cm/s (14 cm/s) in 1993 to 24 cm/s (21 cm/s) in 2008. The RMS difference expressed in percentage of the buoy velocity standard deviation is found to be stable throughout the period (around 60% for the zonal component and 70% for the meridian component).

4.3. Discussion of the b and θ Parameters' Spatial and Temporal Variability

[39] The annual (b_{year} and θ_{year}) and monthly (b_{month} and θ_{month}) parameters shown in Figure 6 present interesting patterns of spatial and temporal variability. The spatial variability may be explained considering the Ekman theory (1905). Indeed, the b and θ parameters can be written as a function of the Ekman depth D_E:

$$b = \frac{\pi\sqrt{2}}{\rho f D_E}e^{\frac{\pi}{D_E}z}, \tag{6}$$

$$\theta = -\frac{\pi}{4} + \frac{\pi}{D_E}z. \tag{7}$$

[40] In equations (6) and (7), z is the vertical level where the Ekman current is computed; in our case, z = −15 m (the drogue's depth of the drifting buoys).

[41] $\theta = \theta_{ek} - \theta_{\tau}$ is negative in the Northern Hemisphere (Ekman currents are directed to the right of the wind direction) and positive in the Southern Hemisphere. There-

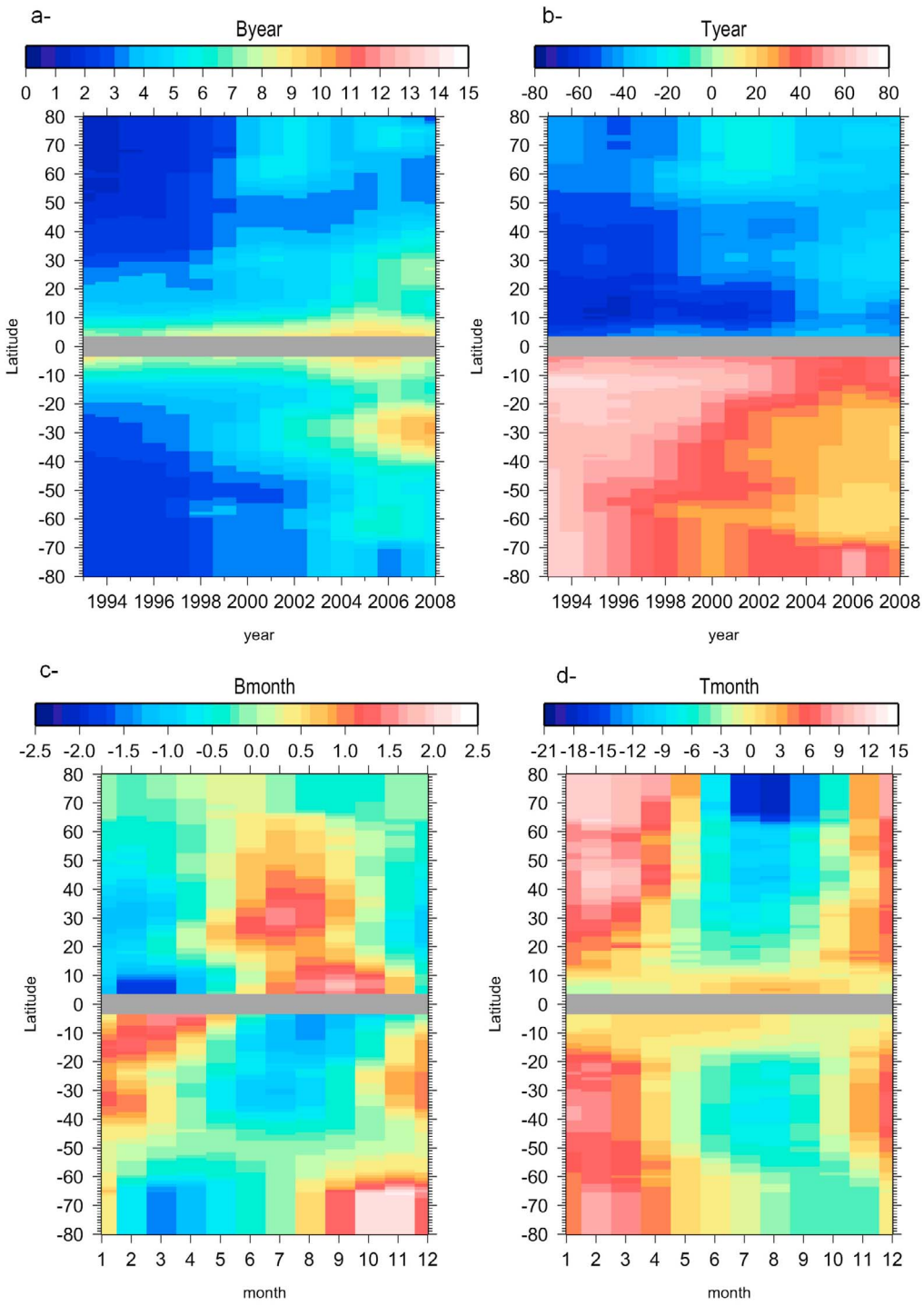

Figure 6. (a, b) Parameters b_{year} and θ_{year} computed by latitudinal bands and year from 1993 to 2008, respectively. (c, d) Parameters b_{month} and θ_{month} computed by latitudinal bands and by month from January (month = 1) to December (month = 12), respectively.

fore, in the Northern hemisphere, $\theta = -\pi\left(\frac{1}{4} + \frac{15}{D_e}\right)$ increases with increasing D_E, leading to decreasing $|\theta|$.

[42] The function $\frac{1}{x}e^{-\frac{1}{x}}$ is decreasing for x > 1. The b coefficient therefore decreases with increasing D_E when $|D_E| > \pi*15$ m.

[43] The increase obtained for each year of both b_{year} and $|\theta_{year}|$ with decreasing latitude (Figures 6a and 6b) is in agreement with increased stratification (and therefore decreased D_E) at low latitudes compared to high latitudes (equations (6) and (7)). Also, both parameters present a clear seasonal cycle with increased b_{month} and increased $|\theta_{month}|$

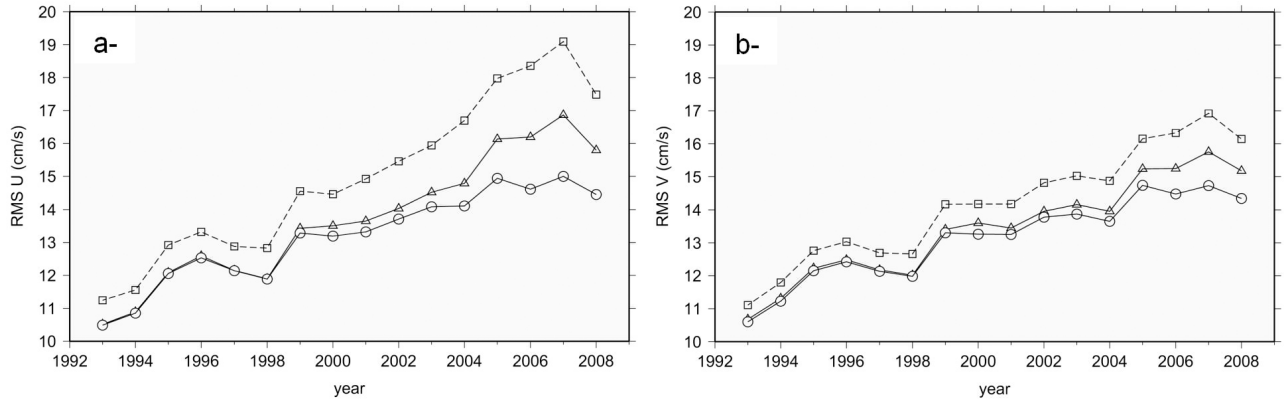

Figure 7. Root-mean-square difference between the geostrophic components of the drifting buoy velocities and the altimetric geostrophic velocities computed by year for the (a) zonal component and (b) meridian component. Triangles show the results obtained when the Ekman model from *Rio and Hernandez* [2003] is used to extract the geostrophic component of the drifting buoy velocities. Circles indicate the results using the new Ekman model computed in this study. Squares show the result obtained when no Ekman current is removed from the drifting buoy velocities.

in summer (Figures 6c and 6d) in good agreement with increased stratification.

[44] The annual trend observed in b_{year} and θ_{year} is more puzzling. Figure 8 shows the yearly magnitude means, computed globally, of the ERA INTERIM wind stresses interpolated along the buoy trajectories (Figure 8a), the raw drifting buoy velocities (Figure 8b) and the altimetric velocities interpolated along the buoy trajectories (Figure 8c). We observe a clear increase from 1993 to 2008 of the drifting buoy velocities magnitude while the intensity of the altimetric velocities remains quite stable all through the period. This indicates an increase from 1993 to 2008 of the ageostrophic component of the ocean currents as measured by the drifting buoys (Figure 8d). There has been throughout the period a steady increase in the number of drifting buoys at high latitudes. This may partly explain the increase in the Ekman current speed, but not fully. High latitudes being characterized by strong winds, the wind stress magnitude interpolated along the buoy trajectory should present a similar trend to that of the ageostrophic current speed, but this is not the case. A maximum in the wind stress magnitude is observed in 1996, as well as an increase from 2000 to 2008. Applying a stationary Ekman model such as that of *Rio and Hernandez* [2003] on the wind stress makes the

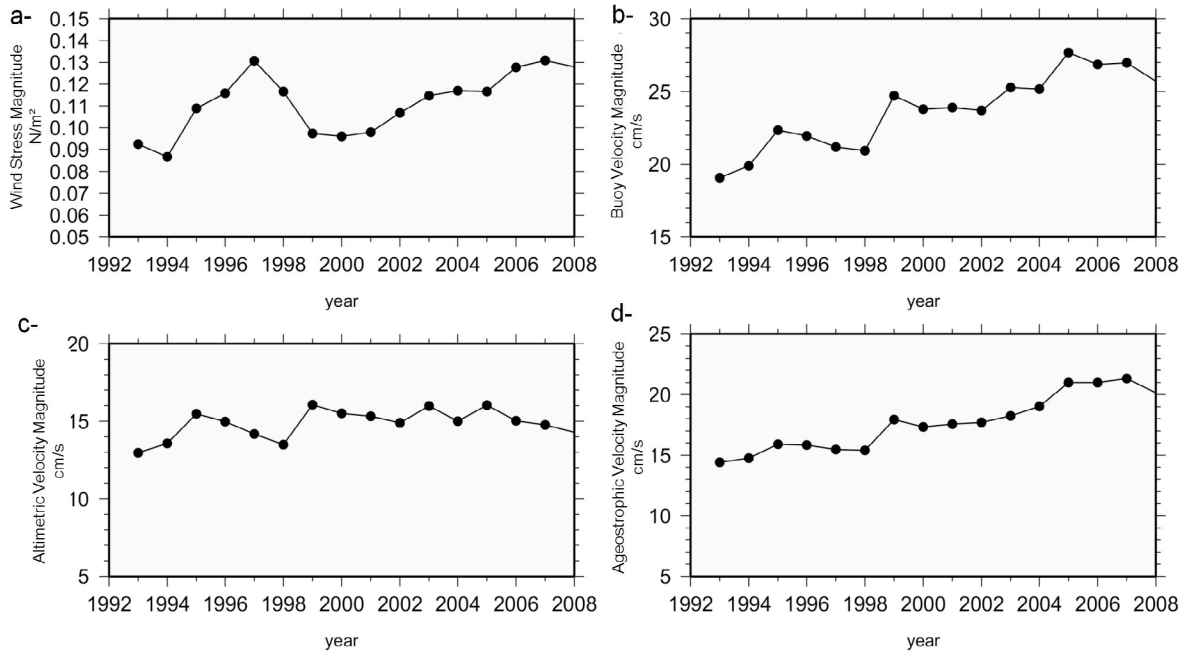

Figure 8. Global magnitude average of (a) the wind stress, (b) the buoy velocities, (c) the altimetric velocities, and (d) the ageostrophic velocities.

corresponding Ekman current magnitude increase from 3 to 5 cm/s only over the 1993–2008 period while the ageostrophic current increases from 14 cm/s to 20 cm/s (Figure 8d). The increase in wind stress magnitude (that may be due from 2000 to 2008 to an increased number of drifters at high latitudes) cannot explain by itself the increased ageostrophic speed of the buoy velocities.

[45] Furthermore, if the better sampling of high latitudes may contribute to the increase of the ageostrophic current speed observed from 1993 to 2008, it does not explain the increase in the b parameter. In effect, we have seen that the b parameter decreases with latitude hand in hand with an increasing D_E. An increased sampling of the high latitudes should therefore result in a decrease with increasing year of the b parameter computed over all latitudes. Instead, when applying the minimization at all latitudes, the b parameter increases from 2.10^{-3} in 1993 to 5.10^{-3} in 2008.

[46] We suggest two possible explanations for this change in the measured drifting buoy velocity magnitudes. First, we might be witnessing a real change in the ocean currents magnitude at 15 m depth, due to an increase in stratification as a response to global warming. The simple Ekman model we use in this study does not allow however this modification to be captured. From equations (6) and (7) a decrease in D_E would result in an increase of both b and $|\theta|$ whereas we observe an increase in b but a decrease in $|\theta|$. The theoretical model from equation (5) was derived for a constant viscosity assumption, which is known to be unrealistic so that a different representation of the Ekman currents may be necessary to fully explain the observed changes in the ageostrophic currents measured by the drifting buoys.

[47] A second possible explanation is a change in the nature of the currents measured by the drifting buoys from 1993 to 2008. The trend may be due to a change in buoy design (a change from SVP drifters to miniSVP drifters has actually occurred in 2004) or to a possible anomaly in the drogue's loss detectors (R. Lumpkin, personal communication, 2009). If the latter is the case, undrogued buoy velocities include a direct wind driven component resulting in a reduced angle to the wind direction (decreased $|\theta|$).

[48] Whatever the explanation (due to buoy technical issues, true ocean currents change, or a combination of both), for which further investigation is still needed, the objective here is to correct the drifting buoy velocities from any ageostrophic signal, in order to be consistent with the measured altimetric geostrophic velocities. We therefore need to take into account this drift in the b and θ parameters.

5. Computation of the CNES-CLS09 MDT

5.1. Synthetic Mean Velocity Data Set and Associated Errors

[49] We use equation (2) to compute the synthetic mean geostrophic velocities at each drifting buoy's position. The drifting buoy velocities are first processed in three steps: First the ERA INTERIM wind stress data are interpolated along the drifting buoy trajectories and the Ekman currents are computed using the model described in section 4. Ekman currents are then subtracted from the drifter's velocities and a further filtering is applied to remove the other ageostrophic components (mainly tidal and inertial currents). The altimetric geostrophic velocity anomalies are then interpolated along the buoy trajectory and subtracted from the geostrophic drifter velocity component. The synthetic mean zonal and meridian velocities are finally averaged into 1/4° boxes (Figures 9a and 9b, respectively). To compute an estimate of the error, we consider each single synthetic observation contained in a 1/4° box to be an independent estimate of the 1/4° box synthetic mean velocity. The standard error on the mean velocity is then computed. This is given, assuming an unbiased estimator of the mean, as the standard deviation of the observations divided by the square root of the number of observations. Errors are displayed in Figure 9c (Figure 9d) for the zonal (meridian) component of the synthetic mean velocity. Away from the western boundary currents and the equatorial band, where they exceed 5 cm/s, errors on the mean are lower than 2–3 cm/s for both components of the velocities.

5.2. Synthetic Mean Heights' Data Set and Associated Errors

[50] The temperature and salinity profiles measured by Argo floats and CTD casts at a given time t and position r were used to compute dynamic heights $Dh(t,r)_{/Pref}$ relative to the profile's reference depth P_{ref}. These dynamic heights reflect the variations of the sea level due to change in density occurring from the surface to the reference level. A difficulty arises when trying to combine them with altimetric anomalies to compute synthetic estimates of the MDT through equation (2). Dynamic heights $Dh(t,r)_{/Pref}$ differ from the requested full dynamical signal by the barotropic component and the deep baroclinic component (owing to density changes from the profile's depth to the bottom). We resolve this difficulty using the following approach.

[51] Any dynamic height computed relative to Pref can be written as the sum of a mean component $\langle Dh \rangle_{/Pref}(r)$ and a time variable component $Dh'_{/Pref}(t,r)$. The time variable component can be linearly related to the full oceanic variability as measured by altimetric Sea Level Anomalies $h'_a(t,r)$ through a regression coefficient $\alpha(Pref,r)$ that depends both on the profile's reference depth and on its geographical location r [*Guinehut et al.*, 2006]. For a given reference depth, the regression coefficient decreases from the tropical band (where it is closer to 1) to high latitudes. Furthermore, for a given geographical location, the regression coefficient increases with increasing reference depth. As an example, Figure 10 shows the regression coefficients obtained for reference depths equal to 200 m and 1900 m. At each in situ profile's time and location, we interpolated the Sea Level Anomaly measured by altimetry and obtained an estimate of the baroclinic component (from the surface to Pref) of the MDT $\langle Dh \rangle_{synth/Pref}(r)$ following:

$$\langle Dh \rangle_{synth/Pref}(r) = Dh_{/Pref}(t,r) - \alpha(p_{ref},r) * h'_a(t,r). \quad (8)$$

[52] For a given reference depth, $\langle Dh \rangle_{synth/Pref}(r)$ differs from the full MDT signal by the mean baroclinic component from P_{ref} to the bottom plus the mean barotropic component. We approximate these two missing components as the difference between the large-scale first guess $\langle h \rangle_{FG}(r)$

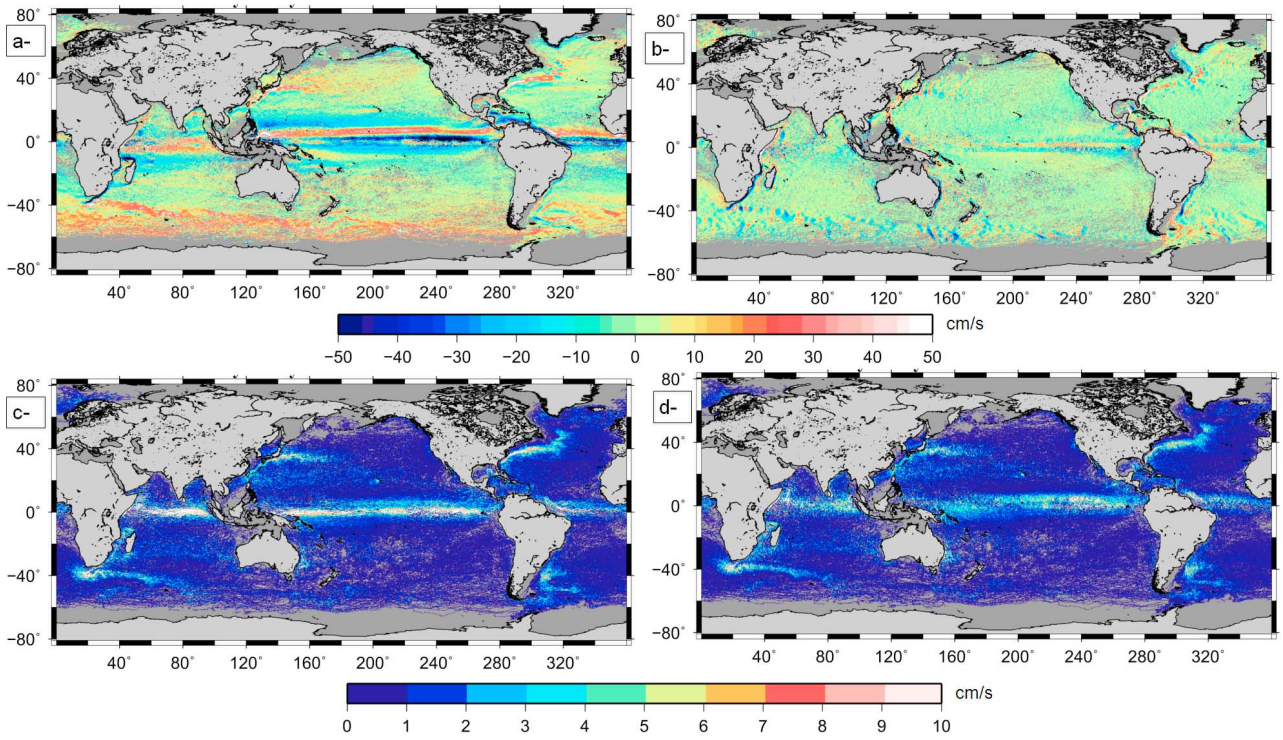

Figure 9. (a, b) Synthetic zonal and meridian mean velocity components (in cm/s) averaged into 1/4° boxes, respectively. (c, d) Error (in cm/s) on the zonal and meridian components of the mean synthetic velocity, respectively.

(computed in section 3 and displayed in Figure 4a) and a climatological estimate of the mean baroclinic component of the circulation relative to P_{ref}, $\langle h \rangle_{WOA05/Pref}(r)$, as given by the WOA05 data set [*Locarnini et al.*, 2006; *Antonov et al.*, 2006]. In doing this, we extract from the large-scale first guess of the 1993–1999 MDT the contribution from the large-scale baroclinic component from the surface to P_{ref}. This approximation does not allow resolving the shortest spatial scales of the mean circulation at P_{ref}, (all spatial scales are theoretically needed to correctly complete $\langle Dh \rangle_{synth/Pref}(r)$). The resulting field is then added to the synthetic estimate of the MDT's baroclinic component $\langle Dh \rangle_{synth/Pref}(r)$ to estimate the MDT's full dynamical signal $\langle h \rangle_{synth}(r)$:

$$\langle h \rangle_{synth}(r) = \langle Dh \rangle_{synth/Pref}(r) + \Big(\langle h \rangle_{FG}(r) - \langle h \rangle_{WOA05/Pref}(r) \Big). \tag{9}$$

[53] Different sources of error pollute the synthetic estimates of the MDT computed above: (1) the error on the altimetric Sea Level Anomalies as provided by AVISO, (2) the errors on the first guess, which is given by Figure 4b, (3) the extraction of the baroclinic variability from the full altimetric ocean variability, (4) the errors on the large-scale

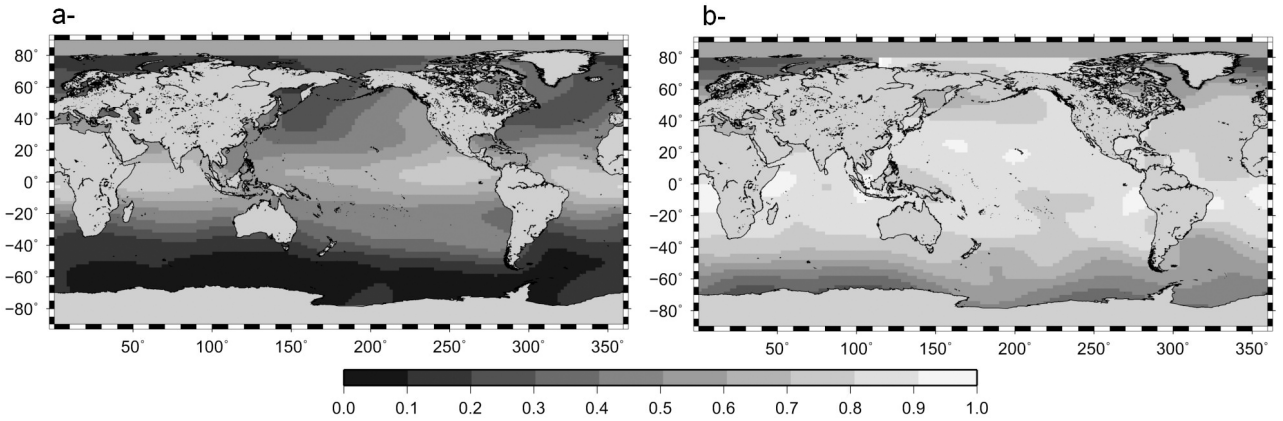

Figure 10. Regression coefficients between in situ dynamic heights relative to (a) 200 m and (b) 1900 m and collocated absolute altimetric heights.

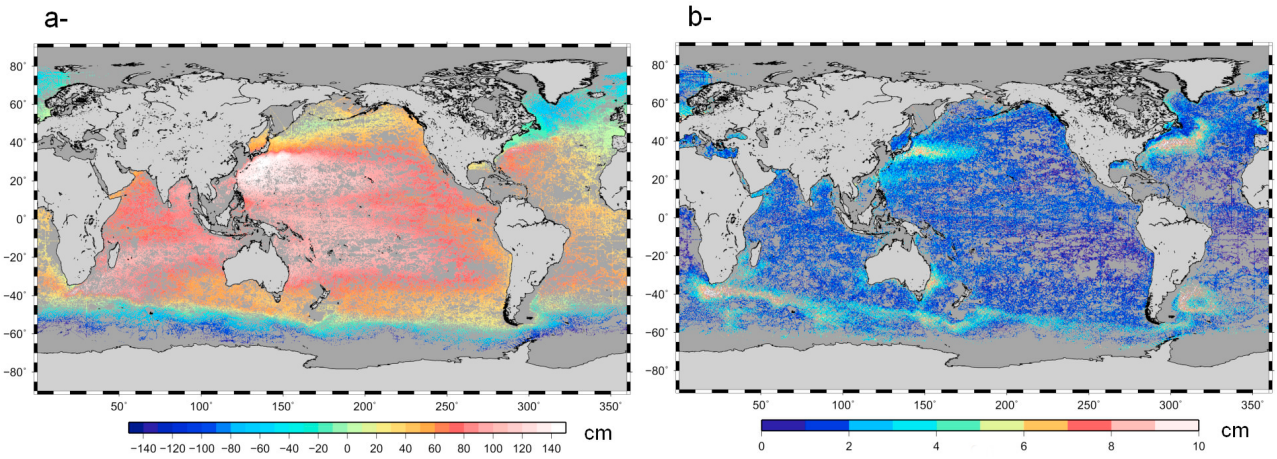

Figure 11. (a) Synthetic mean heights averaged in 1/4° boxes and (b) associated estimated error.

mean baroclinic circulation relative to P_{ref} for the 1993–1999 period as estimated by the WOA05 data set (characterized by a different time period and by larger-scale structures than the optimally filtered first guess), and (5) the omission errors due to the unknown short scales of the mean circulation at P_{ref}.

[54] We approximate these last three error sources as $[1 - \alpha(\text{Pref,r})]*\sigma^2(\text{r})$ with $\sigma^2(\text{r})$ being the variance as computed in section 3 from the a priori GLORYS MDT solution: In strongly baroclinic areas and for profiles measured down to a deep reference depth, the computed synthetic mean dynamic height correctly captures the total MDT variability and the error on the synthetic mean height is small. In contrast, in strongly barotropic areas, or for shallow reference depths, the computed synthetic mean dynamic height misses part of the total MDT variability and consequently the errors are greater.

[55] Finally, the synthetic mean heights and error estimates are averaged into 1/4° boxes (where a simple quadratic sum of all error components is applied). The resulting data set is shown in Figure 11a. Errors of up to 10 cm are found in western boundary currents and in the Antarctic Circumpolar Current while in low-variability areas, the errors are lower than 2 cm (Figure 11b).

5.3. Objective Mapping of the High-Resolution MDT and Associated Mean Geostrophic Currents

[56] The synthetic estimates of the MDT heights and associated velocities computed in sections 5.1 and 5.2 are finally used to improve the first guess computed in section 3 by an optimal filtering method through a multivariate objective analysis, which is a generalization of the formulation written in equation (3). Outside the equatorial band, a linear relationship (i.e., geostrophy) links the mean dynamic height and the mean geostrophic velocities. As a consequence, the correlation function between the mean heights and the mean velocities can be deduced by the derivation of the MDT correlation function C(r) (see Appendix A from *Rio and Hernandez* [2004]). Equation (3) can therefore be applied to estimate, in any point of a 1/4° resolution grid, the MDT and the mean geostrophic currents as a weighted sum of the synthetic mean heights and the synthetic mean velocities. The large-scale first guess computed in section 3 is first removed from the synthetic mean estimates (to reduce the observations means) and added back to the estimated field after inversion.

[57] In the equatorial band, the Coriolis parameter tends toward zero and the correlation functions between heights and geostrophic velocities are no longer valid. For latitudes within 3° of the equator we therefore estimate the MDT from synthetic mean heights only (no velocity information) and the mean velocities from synthetic mean velocities only (no synthetic mean height information).

[58] As stated in section 3, the practical application of this optimal interpolation method necessitates the a priori knowledge of the spatial characteristics (variance and correlation radii) of the residuals between the MDT and the first guess.

[59] The parameters needed for this analysis are therefore the variance and covariance function of the MDT scales shorter than 400 km (which we assume is roughly the spatial resolution of the first guess). As in section 3, these parameters were obtained using as a priori field the GLORYS MDT scales shorter than 400 km. After applying a 2000 km cutoff length filter, maximum values of zonal (meridian) correlation radius of 500–700 km (250–350 km) are obtained in the tropical band. Lower values (lower than 500 km in zonal, 300 km in meridian) are obtained at mid and high latitudes as well as in coastal areas. As in section 3, we have checked the impact of using an alternative a priori MDT based on the OCCAM model to compute the MDT correlation radii. Major differences are obtained in the tropical and equatorial bands, the correlation radii computed with OCCAM being slightly greater than those computed with GLORYS (up to 800 km in zonal and 400 km in meridian). However, the impact on the final solution is, again, very small. (Mean difference of −0.3 mm and RMS difference of 6 mm are obtained in the [15°S–15°N] latitudinal band, where impact is maximal.)

[60] The CNES-CLS09 MDT is finally computed on a 1/4° grid as output of the multivariate objective analysis of the synthetic mean estimates (Figure 12). It will be further discussed and validated in section 6. Furthermore, formal error estimates are computed from the multivariate objective

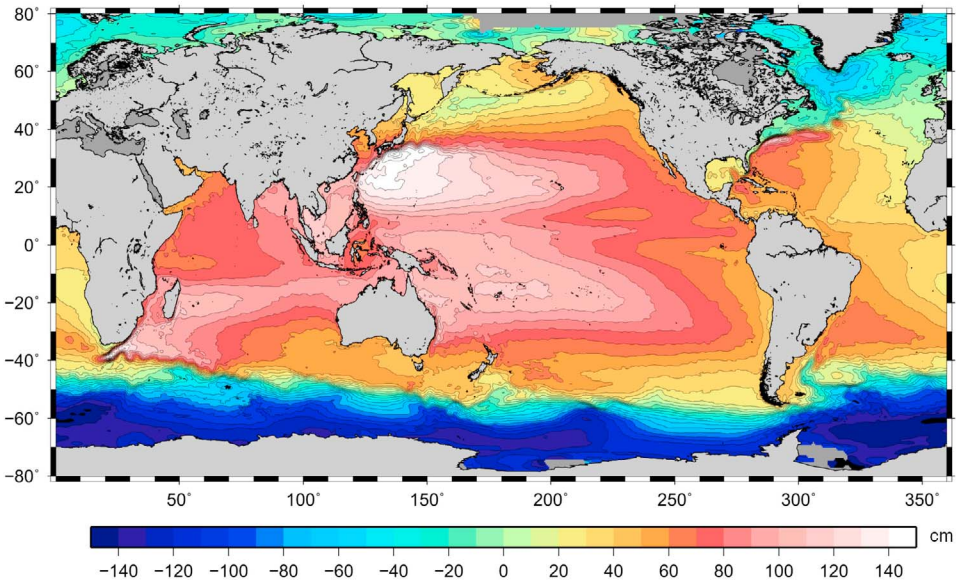

Figure 12. CNES-CLS09 MDT as computed in this study.

analysis (equation (4)). Errors on the MDT are shown in Figure 13. They reach a maximum in western boundary currents (4–5 cm).

[61] The advantage of this method is that the zonal and meridian components of the mean geostrophic circulation (and associated errors) are directly obtained as outputs of the objective analysis on the 1/4° grid, including in the equatorial band. The resulting mean geostrophic currents will be shown and validated for specific areas in section 6.

[62] In section 3, we have made the assumption that the geoid model is stationary (no time variation). Consequently, the time period of the computed first guess depends on the time period over which the altimetric CLS01 Mean Sea Surface is computed (1993–1999). Similarly, altimetric Sea Level Anomalies used in this study are referenced to the 1993–1999 period (section 2.2). Consequently, the mean heights and velocities obtained through equation (2) represent by construction the 1993–1999 mean, independently from the actual in situ measurement time (spanning from 1993 to 2008).

[63] The MDT estimates obtained through either the direct or the synthetic methods are therefore consistent and correspond to estimates of the 1993–1999 mean. The CNES-CLS09 MDT computed in this paper therefore represents the mean of the ocean dynamic topography for the period 1993–1999. It can be used as reference field to reconstruct the absolute dynamic topography from altimetric anomalies computed relative to the same 1993–1999

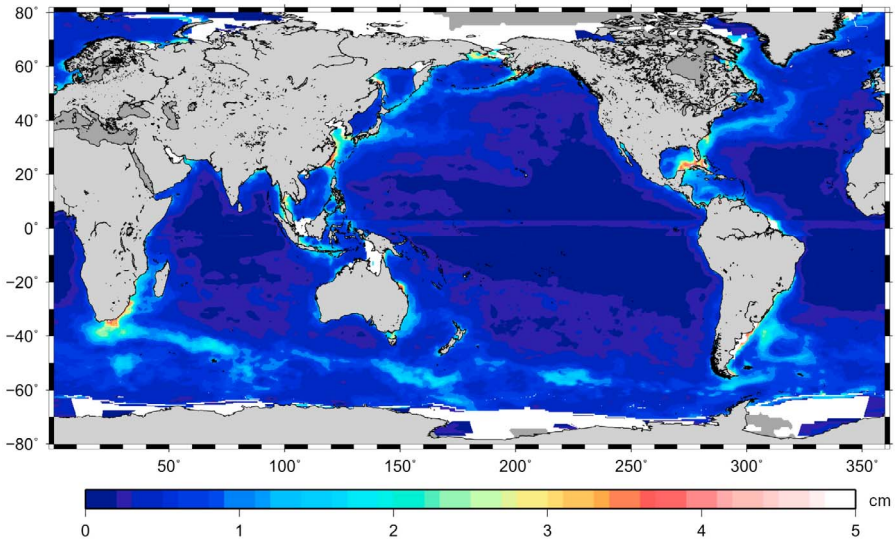

Figure 13. Formal error on the CNES-CLS09 MDT as obtained as output of the multivariate objective analysis.

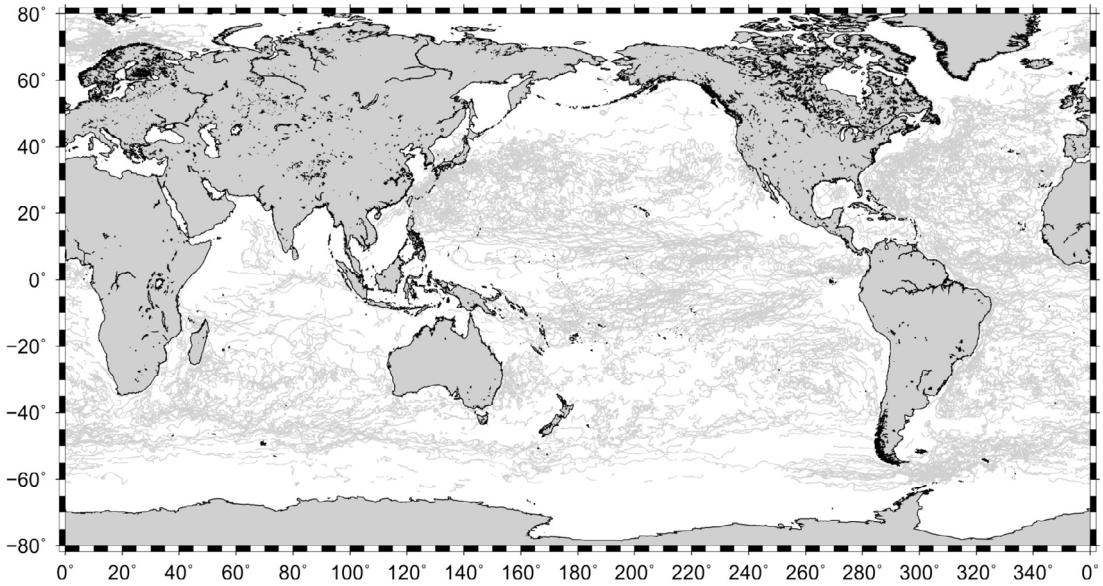

Figure 14. Trajectories of drifting buoys available from January 2009 to February 2010.

mean, as in the case of, for example the AVISO SLA described in section 2.2.

6. Discussion

6.1. Quantitative Assessment of MDTs' Accuracy

[64] In sections 6.2–6.5, we will discuss the quality of the computed CNES-CLS09 MDT by comparing it to other MDT estimates. In addition to qualitative considerations, we try to provide a more quantitative assessment of the different MDTs' accuracy. We consider a data set of drifting buoy velocities measured from January 2009 to July 2010 and delivered in real time by the Coriolis data center. These data were not used in the computation of the CNES-CLS09 MDT and constitute therefore an independent validation data set. The spatial distribution of the independent drifting buoy trajectories is shown in Figure 14. It is rather uniform over the global ocean, which enables us to validate the obtained global MDT almost everywhere (apart from the highest latitudes of the Antarctic Circumpolar Current, where the velocities are less well sampled). To assess the quality of a MDT solution, we proceed as was done in section 3. On the one hand, we compute absolute maps of altimetric heights by adding the MDT grid to the maps of Sea Level Anomalies available weekly over the 2009–2010 time period. We then obtain maps of altimetric geostrophic velocities that we interpolate at the time and location of the drifting buoy velocity measurements. On the other hand, the geostrophic component of the drifting buoy velocities is extracted by using the Ekman model developed in section 4 and by then applying a 3 day low-pass filter. Finally, we compute the root-mean-square (RMS) differences, the vectorial correlation coefficient Rc and the regression slope Au (Av) between the buoys zonal (meridian) geostrophic velocities and the altimetric zonal (meridian) geostrophic velocities. These statistics can be calculated with any existing MDT solution and compared one to each other (over the different MDTs overlapping area). For a given MDT, the obtained RMS is the sum of three main contributions, the MDT velocity errors, the altimetric velocity anomaly errors and the geostrophic buoy velocity errors (including mainly the buoy velocity measurement errors and the Ekman model error). Depending on the region, the last two contributions may well dominate the obtained RMS value. In that case, a strong reduction in the MDT velocity error may result in a weak RMS reduction. For example, if the altimetric and buoy velocity errors represent 75% of the obtained RMS for a given MDT, a reduction of the MDT velocity error from 5 cm/s to 4 cm/s (20%) will decrease the RMS from 10 cm/s to 9.5 cm/s only. In contrast, if the altimetric and buoy velocity errors represent 25% of the obtained RMS for a given MDT, a RMS reduction from 10 cm/s to 9.5 cm/s is obtained if the MDT error reduces from 8.7 cm/s to 8 cm/s (7%). Keeping this in mind, we consider in the following one MDT solution to be "more accurate" than another if we end up with reduced RMS differences to observations, as well as higher vectorial correlation coefficients.

6.2. Impact of the Different in Situ Data Sets Used for the CNES-CLS09 MDT Computation

[65] Three types of in situ data have been used to compute the CNES-CLS09 MDT. To investigate the specific contribution of each data type, three extra runs have been performed in which the synthetic observations used to improve the first guess are based on CTD profiles only (CNES-CLS09-CTD solution), on CTD profiles and Argo floats only (CNES-CLS09-CTD-Argo solution) and on drifting buoy velocities only (CNES-CLS09-Buoy solution). The statistical results of the comparison between altimetric velocities obtained using these different MDT versions and the 2009–2010 geostrophic velocity data set are given in Table 1. With the CNES-CLS09-CTD MDT, a RMS difference of 12.8 cm/s (12 cm/s) is found for the zonal (meridian) component of the velocity. When both CTD and

Table 1. RMS Differences and Vectorial Correlation Coefficient, Rc, Between Altimetric Geostrophic Velocities Computed Using Different Versions of the CNES-CLS09 MDT and the Geostrophic Velocities Computed From the 2009–2010 Drifting Buoy Data Set[a]

	CNES-CLS09-CTD	CNES-CLS09-CTD-Argo	CNES-CLS09-Buoy	CNES-CLS09
DIFF RMSU (cm/s)	12.8	12.6	12.2	11.8
DIFF RMSV (cm/s)	12.0	11.8	11.5	11.3
Rc	0.73	0.74	0.76	0.78

[a]The 2009–2010 drifting buoy data set has 845,130 velocity measurements. RMS differences are shown both for the zonal (DIFF RMSU) and meridional (DIFF RMSV) velocity components.

Argo floats are used (CNES-CLS09-CTD-Argo), these RMS values are reduced to 12.6 cm/s (11.8 cm/s). With the CNES-CLS09-Buoy solution, built only with synthetic mean velocities, the zonal (meridian) RMS difference to observations drops to 12.2 cm/s (11.5 cm/s). Best values however are obtained when all three data types are used (CNES-CLS09 solution). The zonal (meridian) RMS difference to observations is 11.8 cm/s (11.3 cm/s).

[66] In agreement with the RMS results, the vectorial correlation coefficient increases from 0.73 with the CNES-CLS09-CTD solution to 0.74 if Argo floats are included in the synthetic mean height computation. This is less than the correlation obtained with synthetic mean velocities only (0.76). The maximum correlation, however, is obtained for the CNES-CLS09 MDT, for which all data (CTD, Argo, drifting buoys) were used (0.78).

[67] These results show the importance of combining the three different in situ observations to obtain the best possible solution. Further to increasing the number of synthetic observations, they have somehow a complementary content. This is illustrated for the Gulf Stream area in Figure 15. The synthetic mean heights computed from the CTD profiles improve the representation of the Gulf Stream current (Figure 15a), increasing the height difference across the stream compared to the first guess (Figure 15d) in particular at 292°E (50 cm increase) and 305°E (30 cm increase), thus increasing the current mean velocity. Also, the circulation in the area from 310°E to 325°E and from 40°N to 55°N, including the Mann Eddy and the northwest corner, is enhanced. In contrast, at the center of the subpolar and subtropical gyres, the circulation in the CNES-CLS09-CTD solution is close to the first guess circulation. This is due to the low number of CTD profiles in these areas (Figure 2). Further strengthening of the currents is obtained when Argo floats are included in the synthetic mean heights computation (Figure 15b). When only synthetic mean velocities are used (Figure 15c) the height difference across the Gulf Stream at 292°E and 305°E is unchanged but the height isolines are tightened, resulting in increased height gradients, and therefore increased mean velocities. The synthetic mean velocities also bring significant information in the Florida current, which is strongly intensified, compared to the first guess and the CNES-CLS09-CTD-Argo field. Sharper gradients are also obtained in the Labrador current, in the North Atlantic drift and around the subpolar gyre. Also, the mean circulation includes much smaller scales than in the CNES-CLS09-CTD-Argo solution. This may in part represent true oceanographic detail, but to some extent it will also reflect short-scale errors in the synthetic mean velocity computation. When all synthetic observations are used (the CNES-CLS09 MDT in this area is displayed in Figure 19a) the height difference across the Gulf Stream as seen by the synthetic mean heights is maintained and the MDT isolines, as seen by the synthetic mean velocities, are tightened. As a result, the velocities are increased compared both to the CNES-CLS09-CTD-Argo and the CNES-CLS09-Buoy solutions. For example at 295°E, 38°N, the mean speed is 60 cm/s in the CNES-CLS09-CTD-Argo solution, 75 cm/s in the CNES-CLS09-Buoy solution and increases to 85 cm/s when both synthetic mean heights and mean velocities are used (Figure 19c). Outside the strong western boundary currents, the combination of the synthetic mean heights and mean velocities slightly smoothes the short scales of the CNES-CLS09-Buoy solution. Since the comparisons to independent observations are improved with the CNES-CLS09 MDT compared to both the CNES-CLS09-CTD-Argo and the CNES-CLS09-Buoy solutions, we believe that the combination of all data types reduces the residual short-scale noise that may be contained in the synthetic velocity observations, while maintaining the strong gradients.

6.3. Mean Velocities in the Equatorial Band

[68] In the equatorial band, where the geostrophic approximation fails, velocities can be derived from the CNES-CLS09 MDT using a second-order approximation as is done by *Lagerloef et al.* [1999]. We compare these velocities (Figure 16a) with the mean velocities obtained as output from our multivariate objective analysis (Figure 16b). In our method, mean velocities are optimally mapped from the synthetic velocity observations, resulting in much stronger equatorial currents and reduced root-mean-square differences relative to the independent in situ geostrophic velocities. In the [−5°, 5°] latitudinal range, RMS differences relative to zonal (meridian) velocities are reduced from 26.6 cm/s (20.6 cm/s) to 23.3 cm/s (19.4 cm/s) and the vectorial correlation coefficient is increased from 0.57 to 0.67.

6.4. Comparison of the CNES-CLS09 MDT to the Previous RIO05 MDT

[69] The new CNES-CLS09 MDT was built as an update of the previous RIO05 MDT. The most impressive improvements are obtained in energetic areas such as the Antarctic Circumpolar Current and all western boundary currents.

[70] The CNES-CLS09 MDT is shown in Figure 17a for the Kuroshio region, Figure 18a for the Aghulas current, and Figure 19a for the Gulf Stream area. The associated geostrophic speeds are shown in Figures 17c, 18c, and 19c, respectively. For comparison, the MDT obtained in the three regions by the previous RIO05 solution is shown in Figures 17b, 18b, and 19b as well as the corresponding mean geostrophic speeds in Figures 17d, 18d, and 19d.

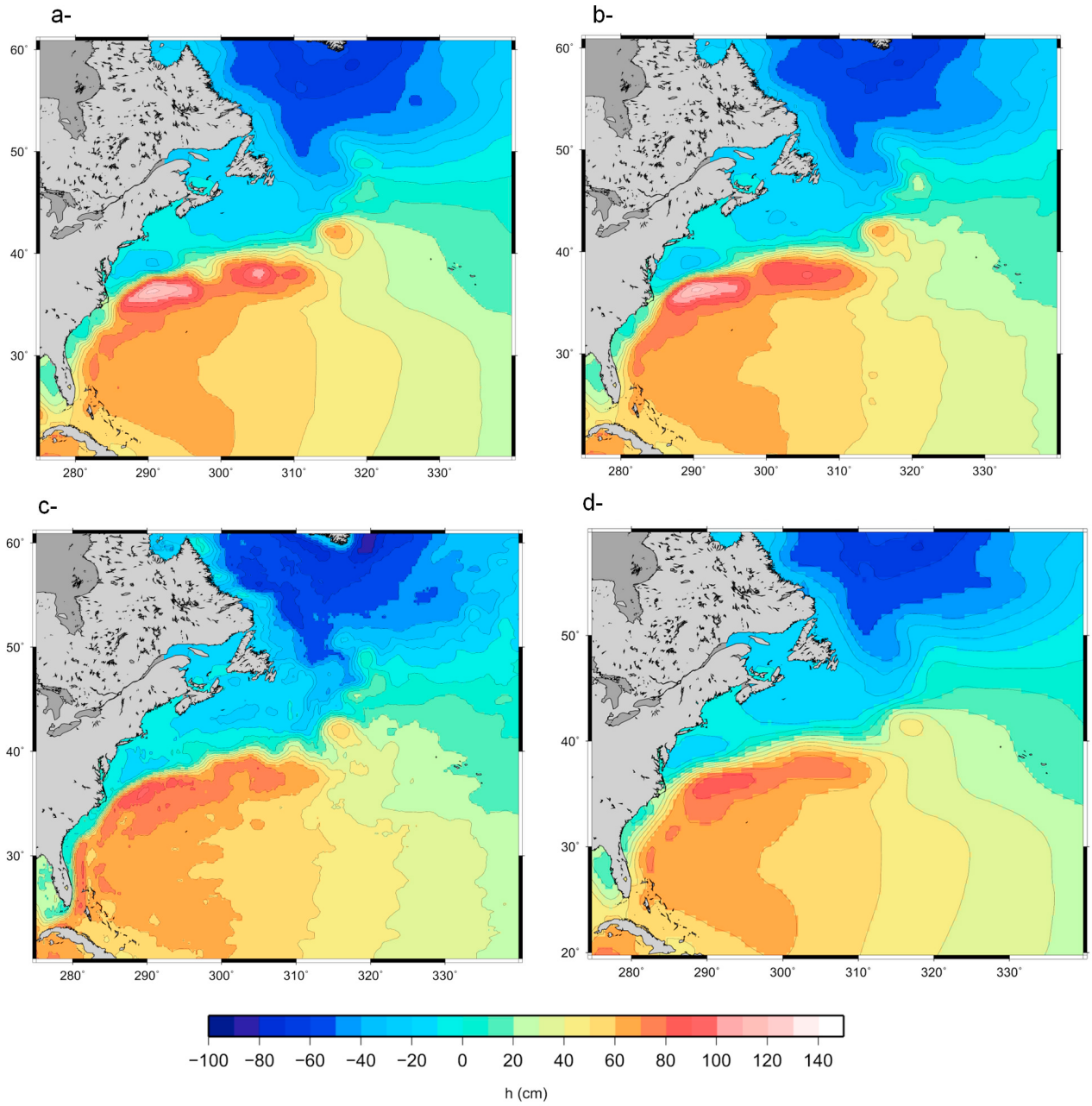

Figure 15. MDT in the Gulf Stream area obtained (a) using synthetic heights from CTD casts only (CNES-CLS09-CTD), (b) using synthetic heights from CTD and Argo profiles (CNES-CLS09-CTD-Argo), (c) using synthetic velocities only (CNES-CLS09-Buoy), and (d) from first guess computed in section 3 by optimal filtering.

[71] In the Kuroshio current (Figure 17) both MDT feature two large anticyclonic meanders centered at 144°E and 150°E and a strong anticyclonic recirculation cell centered at 137°E 33°N, whose northern part corresponds to the maximum velocity amplitude of the Kuroshio current. A 30% increase of this maximum velocity amplitude is obtained in the new CNES-CLS09 solution (120 cm/s) compared to the previous RIO05 field (90 cm/s). Weaker currents such as the Kamtchatka and the Oyashio currents (flowing southward from the Bering Strait toward Japan) are stronger (mean velocities reaching 30 cm/s) and better resolved in the new solution. Also, the mean circulation in the Sea of Japan and the Yellow Sea is much better defined in the new solution. In particular, the Tsushima current, a warm branch from the Kuroshio current flowing northward along the western Japanese coasts, is resolved in the CNES-CLS09 MDT.

[72] Improvements are also clearly visible in the Aghulas current area (Figure 18). The mean circulation around the Madagascar Island is much better resolved, with the signature of the East Madagascar Current, flowing southward along the island's east coast, and the South Equatorial Current,

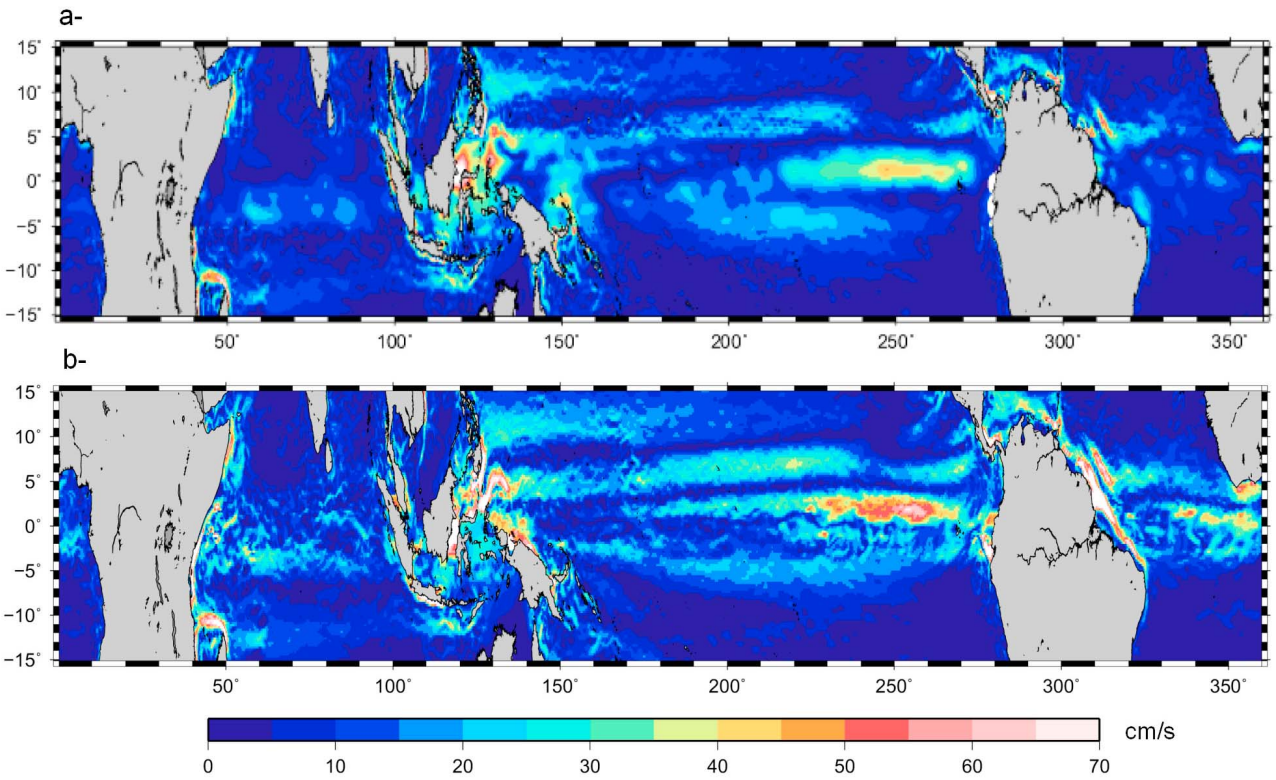

Figure 16. The ocean mean currents in the equatorial band (a) derived from the CNES-CLS09 MDT using the equatorial geostrophic approximation and (b) estimated from the multivariate objective analysis.

accelerating when reaching the northern tip of the island (up to 1 m/s), at around 13°–10°S, before reaching the African coasts where it divides into a northward flowing branch, the East Africa Coastal Current and a southward flowing branch, the Aghulas Current, for which an increase of more than 100% of the maximum velocity amplitude (observable along the southern coast of Africa between 32°S and 36°S) is obtained between the RIO05 solution (70 cm/s) and the CNES-CLS09 field (150 cm/s). The new field also features the signature (visible at 33°S, 6°E and 35°S, 12°E) of the numerous anticyclonic rings that are known to detach from the western tip of the Aghulas retroflexion and propagate northwestward in the Atlantic Ocean.

[73] In the Gulf Stream current (Figure 19), the new CNES-CLS09 MDT features two large anticyclonic recirculation cells on the southern side of the main jet (centered at 290°E, 36°N and 305°E, 37°N) as well as one cyclonic recirculation cell on the northern side of the jet (centered at 290°E, 38°N). The maximum speed in the Gulf Stream region occurs in the Florida current at 29°N in the new field (1.5 m/s), at a position that was not resolved in the RIO05 solution (the current flowing very close to the coast). In the Gulf Stream, a 50% increase of the maximum velocity is observed (up from 80 cm/s in RIO05 to 120 cm/s in the CNES-CLS09 MDT) just upstream of Cap Hatteras. Other boundary currents such as the Labrador current and the South Greenland current are also much better defined in the new field.

[74] The statistical comparisons to independent velocities obtained with the CNES-CLS09 MDT compared to the RIO05 MDT are given in Table 2 for the Kuroshio area, Table 3 for the Aghulas current, and Table 4 for the Gulf Stream area. Compared to the results obtained with the RIO05 solution, regression slopes obtained with the CNES-CLS09 MDT are closer to 1, both for the zonal and the meridian components of the velocity. This is due to the clear sharpening of the MDT gradients in all western boundary currents, resulting in a significant increase in the mean geostrophic velocity amplitude as discussed above. Regression slopes however still remain under 0.7, highlighting the fact that the in situ geostrophic velocities are stronger than the absolute altimetric velocities. This may be due to the coarse spatial and temporal resolution of the altimetric Sea Level Anomalies (1 week, 100 km), insufficient to fully resolve the ocean variability.

[75] The RMS differences obtained with the CNES-CLS09 MDT are also reduced for both components of the velocity compared to the RMS values obtained with the RIO05 MDT, and the correlation coefficient is increased.

[76] In Tables 2–4, the results obtained with the first guess in each region are also given for comparison. The reduced RMS differences to observations, coupled with the higher correlation coefficients demonstrate the significant impact of the synthetic estimates for resolving the spatial scales of the MDT down to 25 km (1/4°), as a complement to the large-scale information from the GRACE derived MDT.

[77] In conclusion, we observe between the old RIO05 solution and the new CNES-CLS09 field a clear sharpening of the MDT gradients in all western boundary currents, resulting in a significant increase in the velocity amplitude

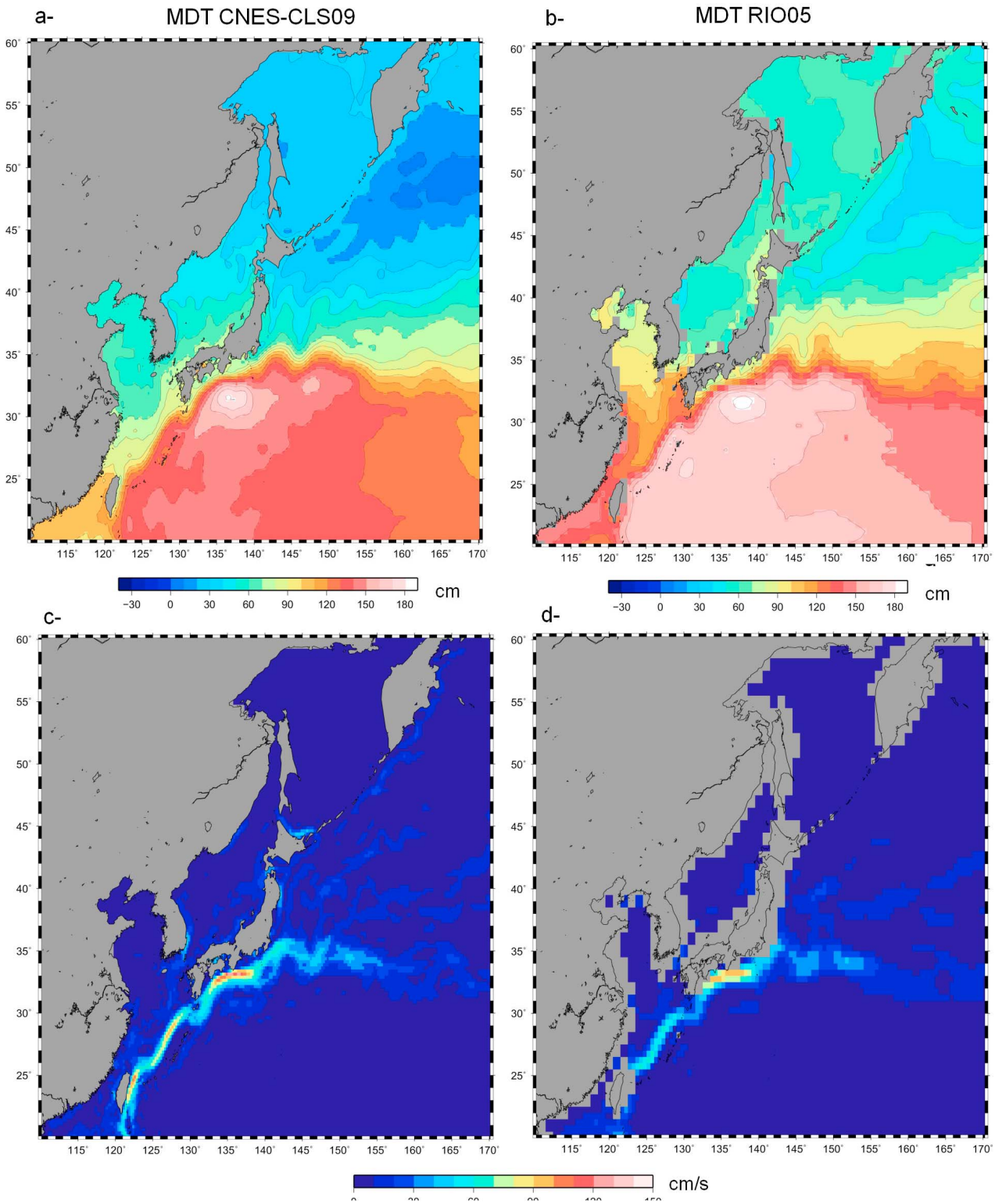

Figure 17. The (a, b) MDT and (c, d) speed of the associated geostrophic currents in the Kuroshio current area. Results are shown for the CNES-CLS09 solution (Figures 17a and 17c) and the RIO05 solution (Figures 17b and 17d).

of the mean geostrophic circulation. This is due to the higher resolution (1/4°) of the CNES-CLS09 MDT compared to the RIO05 MDT (1/2°). It is worth recalling at this point that the synthetic mean heights and mean velocities used for the RIO05 MDT estimation had also been computed into 1/4° boxes [*Rio et al.*, 2005]. However, the error on each synthetic mean (computed as the 1/4° box variance divided by the number of observations)

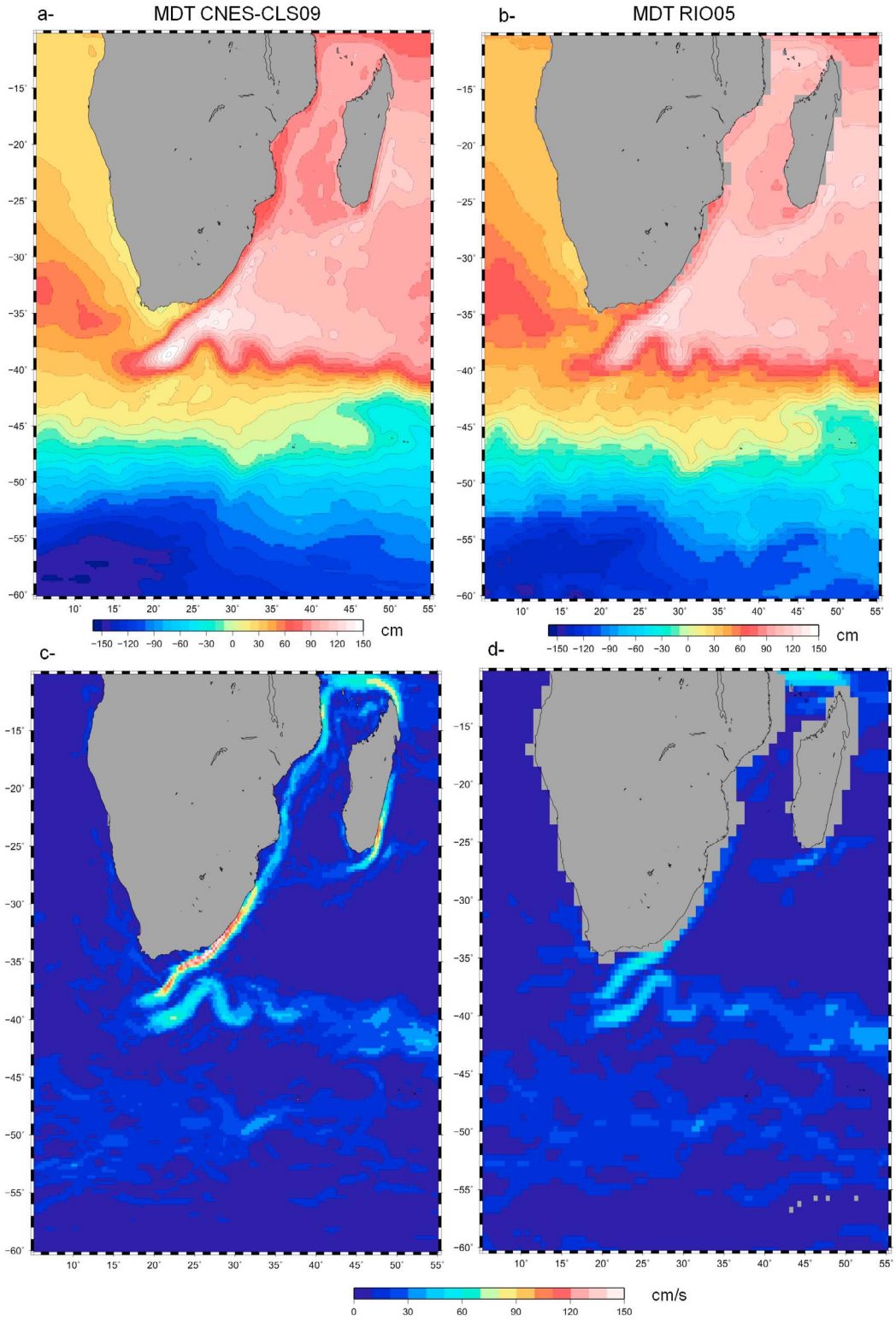

Figure 18. The (a, b) MDT and (c, d) speed of the associated geostrophic currents in the Aghulas current area. Results are shown for the CNES-CLS09 solution (Figures 18a and 18c) and the RIO05 solution (Figures 18b and 18d).

was much higher than the errors on the synthetic means entering the CNES-CLS09 MDT, for which far more data are available (Figures 1 and 2). The true resolution of the MDT is given by the intrinsic resolution of the observations used in input, not by the arbitrarily chosen output grid spacing. As a consequence, computing the RIO05 MDT on a 1/4° resolution grid does not change anything. In particular, the comparison to independent observations gives the

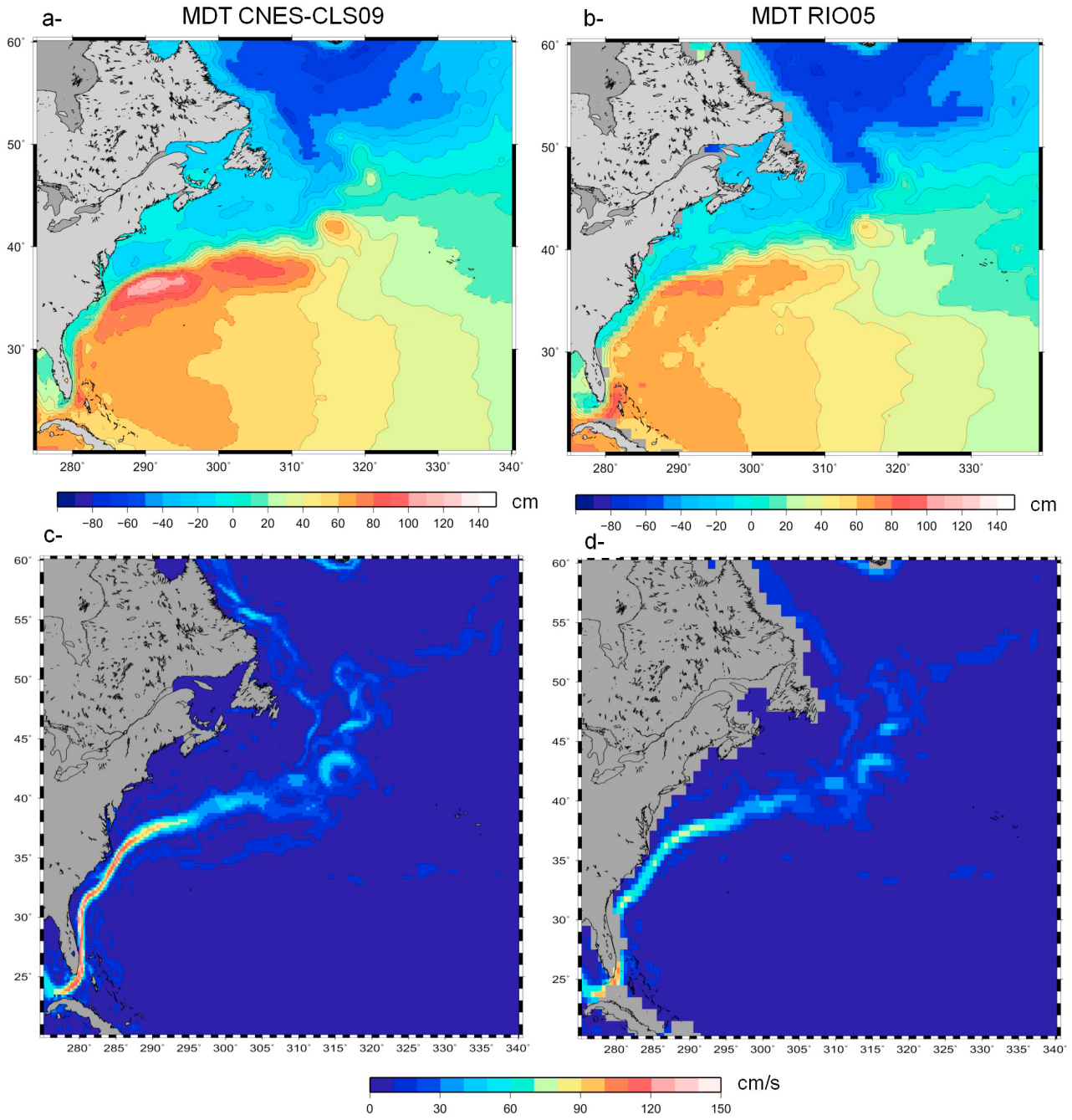

Figure 19. The (a, b) MDT and (c, d) speed of the associated geostrophic currents in the Gulf Stream current area. Results are shown for the CNES-CLS09 solution (Figures 19a and 19c) and the RIO05 solution (Figures 19b and 19d).

Table 2. RMS Differences and Vectorial Correlation Coefficient, Rc, Between Altimetric Geostrophic Velocities Computed Using Different MDTs and 60,156 Geostrophic Velocities Computed From The 2009–2010 Drifting Buoy Data Set in the Kuroshio Current Area[a]

	CNES-CLS09	RIO05	MAX09	GLORYS	DNSC08	VM08HR	First Guess
DIFF RMSU (cm/s)	14.6 (14.3)	15.3	15.1	14.9	15.4	15.5	16.5
DIFF RMSV (cm/s)	15.0 (14.9)	16.0	15.7	15.6	16.2	16.3	17.5
Au	0.69 (0.71)	0.64	0.63	0.66	0.66	0.66	0.57
Av	0.64 (0.66)	0.59	0.58	0.63	0.61	0.61	0.51
Rc	0.83 (0.83)	0.81	0.82	0.82	0.80	0.80	0.77

[a]The Kuroshio current area is between longitudes 110°E and 170°E and between latitudes 20°N and 60°N. RMS differences are shown both for the zonal (DIFF RMSU) and meridional (DIFF RMSV) velocity components.

Table 3. RMS Differences and Vectorial Correlation Coefficient, Rc, Between Altimetric Geostrophic Velocities Computed Using Different MDTs and 37,348 Geostrophic Velocities Computed From the 2009–2010 Drifting Buoy Data Set in the Aghulas Current Area[a]

	CNES-CLS09	RIO05	MAX09	GLORYS	DNSC08	VM08HR	First Guess
DIFF RMSU (cm/s)	13.0 (12.9)	13.4	13.2	13.4	13.9	13.8	14.1
DIFF RMSV (cm/s)	12.6 (12.4)	13.1	12.8	12.8	14.2	13.9	14.1
Au	0.67 (0.68)	0.63	0.64	0.65	0.65	0.65	0.60
Av	0.65 (0.66)	0.63	0.64	0.65	0.62	0.61	0.58
Rc	0.85 (0.86)	0.85	0.85	0.85	0.82	0.82	0.82

[a]The Aghulas current area is between longitudes 5°E and 55°E and between latitudes 60°S and 10°S. RMS differences are shown both for the zonal (DIFF RMSU) and meridional (DIFF RMSV) velocity components.

same results. For the CNES-CLS09 MDT, the higher number of data available for the computation, coupled with improved processing, has allowed us to compute synthetic estimates in 1/4° boxes with a much reduced error level. We have therefore been able to estimate the final solution on a 1/4° resolution grid which has resulted in increased mean current velocities together with much better defined jets, and a better description of the mean currents along the coasts.

[78] As described in section 5.3, the mean geostrophic velocities corresponding to the CNES-CLS09 MDT have also been obtained as output from the multivariate objective analysis. They slightly differ from the geostrophic velocities computed a posteriori by simple differentiation of the mean height field. The statistical comparisons obtained using the optimally derived mean velocities are indicated in Tables 2–4 between parentheses. This systematically leads to further slight improvements of the results (reduced RMS differences are obtained, as well as increased vectorial correlation).

6.5. Comparison of the CNES-CLS09 MDT to Other Existing MDT Solutions

[79] Finally, we have compared the CNES-CLS09 MDT to a number of global mean dynamic topographies that have been computed recently.

[80] 1. The DNSC08 MDT was computed by *Andersen and Knudsen* [2009] using the recent EGM08 geoid model [*Pavlis et al.*, 2008], together with the DNSC08 altimetric MSS. They further filtered the obtained MDT to keep only the spatial scales greater than 75 km. The DNSC08 MDT was computed for the 1993–2004 time period.

[81] 2. The VM08HR MDT was computed by *Vianna and Menezes* [2010] using the recent EGM08 geoid model [*Pavlis et al.*, 2008], together with the DNSC08 altimetric MSS. Applying Singular Spectrum Analysis, they obtained a global MDT on a 1/10° resolution grid, for the period 1993–2004.

[82] 3. The MAX09 MDT was computed on a 1/2° regular grid by *Maximenko et al.* [2009] using the GGM02C geoid model from *Tapley et al.* [2003], the GSFCMSS00 Mean Sea Surface, and an updated data set of drifting buoy velocities compared to their previous work [*Maximenko and Niiler*, 2005]. The MAX09 MDT was computed for the 1993–2002 time period.

[83] 4. The GLORYS MDT comes from an Ocean General Circulation Model assimilating altimetric and in situ data, already described in section 3. It corresponds to the 1993–2002 time period.

[84] The four solutions listed above were computed relative to different time periods. For validation purpose, all four were adjusted to the CNES-CLS09 MDT time period (1993–1999) by removing the average, computed over their time period, of the AVISO altimetric Sea Level Anomalies (which are computed relative to a 1993–1999 mean profile).

[85] Comparison results to the data set of independent geostrophic velocities are given for the three areas detailed above (the Kuroshio current area, the Aghulas current area, and the Gulf Stream area) in Tables 2–4, respectively. In all three areas, improved results are obtained with the CNES-CLS09 MDT compared to the other existing MDT solutions. Whereas the scores obtained with the CNES-CLS09 MDT, the GLORYS MDT and the MAX09 MDT are rather close to each other, the major improvements are observed when comparing the CNES-CLS09 MDT to the MDTs computed using the highest-resolution geoid model available currently, EGM08. These MDT are computed on very high resolution grids (0.1° for the VM08HR MDT, 1′ for the DNSC08 MDT, although a 75 km filter was applied). For example, in the Kuroshio area (Table 2), root-mean-square differences of 15.4 cm/s (16.2 cm/s) are obtained between the DNSC08 mean zonal (meridian) velocities, compared to 15.5 cm/s (16.3 cm/s) for the VM08HR solution and to 14.6 cm/s (15 cm/s) for the CNES-CLS09 solution. To

Table 4. RMS Differences and Vectorial Correlation Coefficient, Rc, Between Altimetric Geostrophic Velocities Computed Using Different MDTs and 113,819 geostrophic Velocities Computed From the 2009–2010 Drifting Buoy Data Set in the Gulf Stream Current Area[a]

	CNES-CLS09	RIO05	MAX09	GLORYS	DNSC08	VM08HR	First Guess
DIFF RMSU (cm/s)	12.3 (12.0)	12.3	12.5	12.3	12.6	12.4	13.4
DIFF RMSV (cm/s)	11.6 (11.6)	11.7	11.8	11.8	12.0	11.9	13.0
Au	0.62 (0.60)	0.57	0.55	0.58	0.59	0.60	0.54
Av	0.58 (0.59)	0.57	0.56	0.57	0.58	0.58	0.54
Rc	0.78 (0.78)	0.78	0.77	0.77	0.76	0.77	0.75

[a]The Gulf Stream current area is between longitudes 275°E and 340°E and between latitudes 20°N to 60°N. RMS differences are shown both for the zonal (DIFF RMSU) and meridional (DIFF RMSV) velocity components.

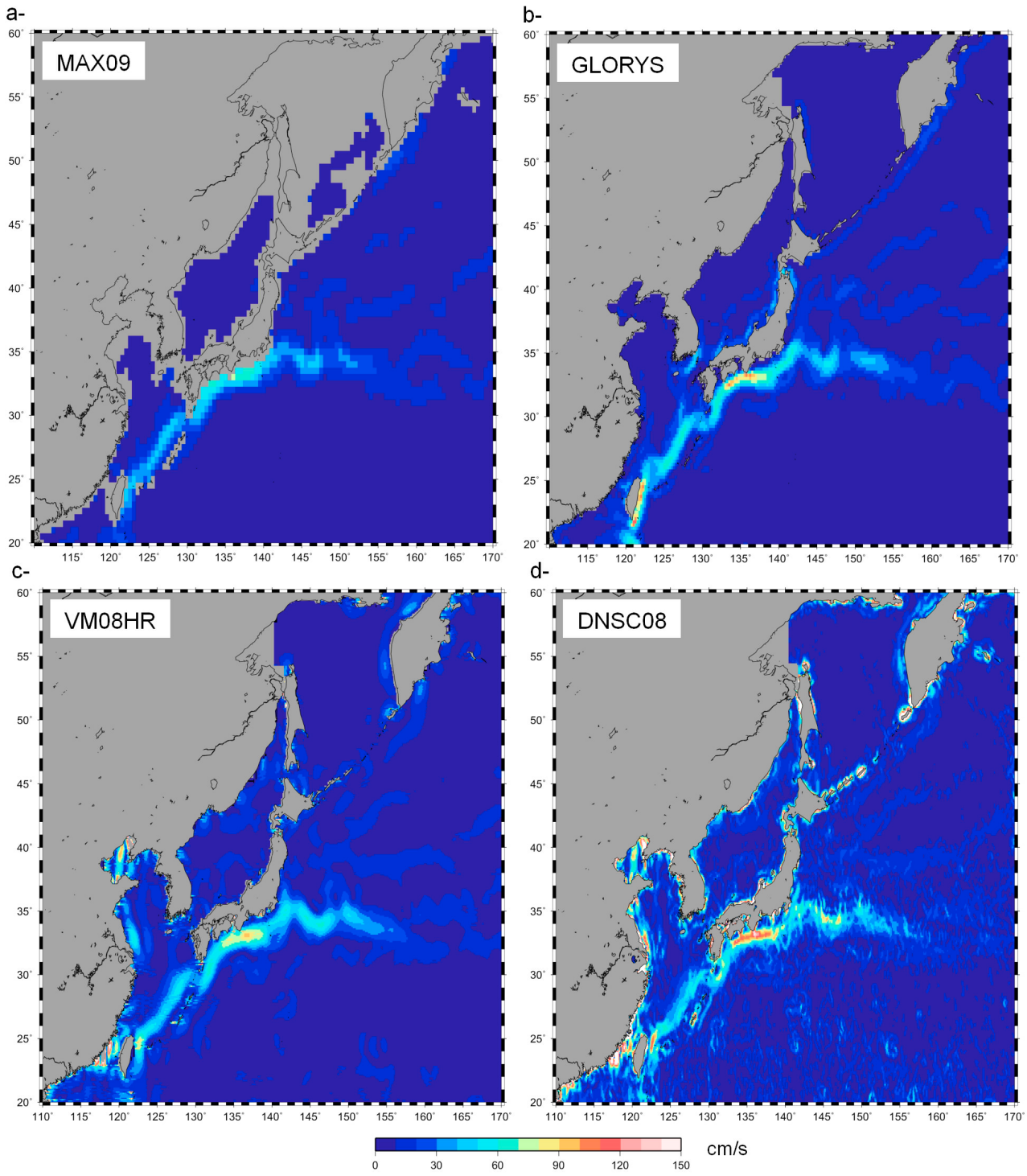

Figure 20. Speed of the mean geostrophic currents computed in the Kuroshio current area from different MDT models: (a) MAX09 MDT, (b) GLORYS MDT, (c) VM08HR MDT, and (d) DNSC08 MDT.

better understand this apparently surprising result, we have displayed in Figure 20 the amplitude of the mean geostrophic velocities in the Kuroshio current area computed from the four different MDT solutions (the MAX09 MDT in Figure 20a, the GLORYS MDT in Figure 20b, the VM08HR MDT in Figure 20c, and the DNSC08 MDT in Figure 20d). The MAX09 MDT, available on a 1/2° resolution grid, is rather smooth, with a maximum velocity amplitude in the Kuroshio of around 70 cm/s. The mean circulation from GLORYS MDT is more intense, in rather good qualitative agreement with the CNES-CLS09 field. Despite the high-resolution grid of 0.1°, the mean circulation depicted in the VM08HR MDT is rather smooth with maximum velocity amplitude reaching 100 cm/s, less than the maximum of 120 cm/s obtained with the CNES-

CLS09 solution and the GLORYS MDT. Higher velocity intensities, of up to 120 cm/s, are obtained in the DNSC08 MDT, which contains shorter scales than the other solutions. Considering the poorer comparison results to independent observations, it is difficult to conclude if these short scales are dominated by real oceanographic signal or noise.

[86] Finally, it is interesting to observe that better results are obtained with the GLORYS MDT than with the RIO05 MDT. As the RIO05 MDT was used for the altimetric data assimilation in the GLORYS reanalysis exercise, this shows the improvements brought by the dynamically consistent assimilation of the in situ T,S profiles, the altimetric data, and the Sea Surface Temperature in global ocean assimilation system for the description of the ocean circulation.

7. Conclusion

[87] In this paper, we have described the calculation of a new global 1/4° MDT (named CNES-CLS09) based on the combination of GRACE data, altimetric measurements and oceanographic in situ data. It is representative of the 1993–1999 time period. The methodology is similar to that described by *Rio and Hernandez* [2004] and *Rio et al.* [2005]. However, this new solution has benefited from a number of significant improvements: (1) the use of a newly computed geoid model, based on 4.5 years of GRACE data (the GRACE geoid model used for the RIO05 MDT computation was based on 2 years of GRACE data), (2) the use of an optimal filtering method to compute the large-scale MDT first guess, instead of the classical Gaussian filter used for the RIO05 first guess computation, (3) the use of an updated data set of drifting buoy velocities (covering the period 1993–2008 instead of 1993–2002), (4) the use of a new Ekman model for extracting the geostrophic velocity component from the drifting buoy velocities, (5) the use of an updated data set of in situ dynamic heights (covering the period 1993–2008 instead of 1993–2002), including the Argo period, (6) the use of an improved methodology for the processing of the dynamic heights, and (7) the computation of mean currents globally, including the equatorial band.

[88] As a result, the new CNES-CLS09 MDT is much improved compared to the previous RIO05 MDT field. All major currents are better resolved and feature much higher intensity, resulting in better consistency when computing altimetric geostrophic currents and comparing them to independent in situ measurements of the surface currents. Improvements are also obtained with the new 1/4° CNES-CLS09 MDT compared to other existing MDT solutions, including the high-resolution MDTs based on the 8 km resolution geoid model EGM08. This demonstrates the advantage of using in situ oceanographic data together with satellite-only geoid models to resolve the shortest scales of the ocean mean circulation.

[89] In addition to the computation of a new global MDT, this work has led to the development of a new model for Ekman current computation. A trend in the mean global intensity of the ageostrophic currents measured by the drifting buoys has been highlighted. However, further investigation is required in order to conclude that this trend is due to the increased Ekman response to wind stress, (through for instance, an increased stratification of the ocean from 1993 to today).

[90] In the near future, the use of GOCE data will enable the geoid to be determined, with centimetric accuracy, to a horizontal resolution of 100 km. The optimal filtering approach applied here for the first guess computation should prove a useful method for estimating the MDT down to spatial scales of 100 km from the direct difference between an altimetric MSS and the GOCE geoid model. Considering the unprecedented accuracy of the MDT at scales greater than 100km, which is expected from the use of GOCE data, the GOCE MDT will tell us more about the accuracy of the CNES-CLS09 MDT at these scales. However, as highlighted by *Maximenko et al.* [2008], up-to-date MDT solutions reveal the presence of high-resolution currents that may not be resolved by GOCE data. We expect that synthetic MDT estimates as computed in this study will still be very helpful, in combination with GOCE-derived MDT, to resolve the MDT on scales shorter than 100 km. This means that the method presented in this paper will provide a good way of improving upon the raw GOCE MDT, with improvements expected especially in coastal currents as well as in western boundary currents, which are particularly important for oceanographic and climate applications, as well as in semi enclosed basins such as the Mediterranean.

[91] **Acknowledgments.** This study was funded by the Centre National d'Etudes Spatiales (CNES, Toulouse, France) in the framework of the SLOOP project. We thank the two anonymous reviewers for their helpful insight and comments on the manuscript.

References

Andersen, O. B., and P. Knudsen (2009), DNSC08 mean sea surface and mean dynamic topography models, *J. Geophys. Res.*, *114*, C11001, doi:10.1029/2008JC005179.

Antonov, J. I., R. A. Locarnini, T. P. Boyer, A. V. Mishonov, and H. E. Garcia (2006), *World Ocean Atlas 2005*, vol. 2, *Salinity*, *NOAA Atlas NESDIS*, vol. 62, edited by S. Levitus, 182 pp., NOAA, Silver Spring, Md.

Arhan, M., and A. Colin de Verdiere (1985), Dynamics of eddy motions in the eastern North Atlantic, *J. Phys. Oceanogr.*, *15*, 153–170, doi:10.1175/1520-0485(1985)015<0153:DOEMIT>2.0.CO;2.

Bingham, R. J. (2010), Nonlinear anisotropic diffusive filtering applied to the ocean's mean dynamic topography, *Remote Sens. Lett.*, *1*, 205–212.

Bingham, R. J., K. Haines, and C. W. Hughes (2008), Calculating the ocean's mean dynamic topography from a mean sea surface and a geoid, *J. Atmos. Oceanic Technol.*, *25*, 1808–1822, doi:10.1175/2008JTECHO568.1.

Bonjean, F., and G. S. E. Lagerloef (2002), Diagnostic model and analysis of the surface currents in the tropical Pacific Ocean, *J. Phys. Oceanogr.*, *32*, 2938–2954, doi:10.1175/1520-0485(2002)032<2938:DMAAOT>2.0.CO;2.

Bretherton, F. P., R. E. Davis, and C. B. Fandry (1976), A technique for objective analysis and design of oceanographic experiments applied to MODE-73, *Deep Sea Res. Oceanogr. Abstr.*, *23*, 559–582.

Bruinsma, S., J. M. Lemoine, R. Biancale, and N. Valès (2010), CNES/GRGS 10-day gravity field models (release 2) and their evaluation, *Adv. Space Res.*, *45*, 587–601, doi:10.1016/j.asr.2009.10.012.

Cheney, R. E., J. G. Marsh, and B. D. Beckley (1983), Global mesoscale variability from collinear tracks of Seasat altimeter data, *J. Geophys. Res.*, *88*, 4343–4354, doi:10.1029/JC088iC07p04343.

Ducet, N., P.-Y. Le Traon, and G. Reverdin (2000), Global high-resolution mapping of ocean circulation from TOPEX/Poseidon and ERS-1 and -2, *J. Geophys. Res.*, *105*, 19,477–19,498, doi:10.1029/2000JC900063.

European Space Agency (1999), The four candidate Earth Explorer core missions: Gravity Field and Steady-State Ocean Circulation Mission, *Rep. ESA SP-1233(1)*, Paris.

Ferry, N., L. Parent, G. Garric, B. Barnier, N. C. Jourdain, and the Mercator Ocean Team (2010), Mercator Global Eddy Permitting Ocean Reanalysis GLORYS1V1: Description and results, *Mercator-Ocean Newsl.*, *36*, 15–27. [Available at http://www.mercator-ocean.fr/documents/lettre/lettre_36_en.pdf.]

Fox, A. D., and K. Haines (2003), Interpretation of water transformations diagnosed from data assimilation, *J. Phys. Oceanogr.*, *33*, 485–498, doi:10.1175/1520-0485(2003)033<0485:IOWMTD>2.0.CO;2.

Fu, L.-L. (2006), Pathways of eddies in the South Atlantic Ocean revealed from satellite altimeter observations, *Geophys. Res. Lett.*, *33*, L14610, doi:10.1029/2006GL026245.

Guinehut, S., P.-Y. Le Traon, and G. Larnicol (2006), What can we learn from global altimetry/hydrography comparisons?, *Geophys. Res. Lett.*, *33*, L10604, doi:10.1029/2005GL025551.

Guinehut, S., C. Coatanoan, A.-L. Dhomps, P.-Y. Le Traon, and G. Larnicol (2009), On the use of satellite altimeter data in Argo quality control, *J. Atmos. Oceanic Technol.*, *26*, 395–402, doi:10.1175/2008JTECHO648.1.

Hansen, D. V., and P.-M. Poulain (1996), Processing of WOCE/TOGA drifter data, *J. Atmos. Oceanic Technol.*, *13*, 900–909, doi:10.1175/1520-0426(1996)013<0900:QCAIOW>2.0.CO;2.

Hernandez, F., and P. Schaeffer (2001), Surface moyenne oceanique: Support scientifique à la mission altimetrique Jason-1, et à une mission micro-satellite altimétrique, *Rapp. CLS/DOS/NT/00.341*, Collect. Localisation Satell., Ramonville Saint-Agne, France.

Hughes, C. W., and R. J. Bingham (2008), An oceanographer's guide to GOCE and the geoid, *Ocean Sci.*, *4*, 15–29, doi:10.5194/os-4-15-2008.

Hunegnaw, A., F. Siegismund, R. Hipkin, and K. A. Mork (2009), Absolute flow field estimation for the Nordic seas from combined gravimetric, altimetric, and in situ data, *J. Geophys. Res.*, *114*, C02022, doi:10.1029/2008JC004797.

Jayne, S. R. (2006), Circulation of the North Atlantic Ocean from altimetry and the Gravity Recovery and Climate Experiment geoid, *J. Geophys. Res.*, *111*, C03005, doi:10.1029/2005JC003128.

Knudsen, P., et al. (2006), GOCINA: Geoid and Ocean Circulation in the North Atlantic—Final report, *Tech. Rep. 5*, Dan. Natl. Space Cent., Copenhagen.

Lagerloef, G. S. E., G. T. Mitchum, R. B. Lukas, and P. P. Niiler (1999), Tropical Pacific near-surface currents estimated from altimeter, wind, and drifter data, *J. Geophys. Res.*, *104*, 23,313–23,326, doi:10.1029/1999JC900197.

Larnicol, G., S. Guinehut, M.-H. Rio, M. Drevillon, Y. Faugere, and G. Nicolas (2006), The global observed ocean products of the French Mercator project, *Rep. ESA SP-614*, Eur. Space Agency, Paris.

LeGrand, P., E. J. O. Schrama, and J. Tournadre (2003), An inverse estimate of the dynamic topography of the ocean, *Geophys. Res. Lett.*, *30*(2), 1062, doi:10.1029/2002GL014917.

Locarnini, R. A., A. V. Mishonov, J. I. Antonov, T. P. Boyer, and H. E. Garcia (2006), *World Ocean Atlas 2005*, vol. 1, *Temperature*, *NOAA Atlas NESDIS*, vol. 61, edited by S. Levitus, 182 pp., NOAA, Silver Spring, Md.

Maximenko, N. A., and P. P. Niiler (2005), Hybrid decade-mean global sea level with mesoscale resolution, in *Recent Advances in Marine Science and Technology, 2004*, edited by N. Saxena, pp. 55–59, PACON Int., Honolulu.

Maximenko, N. A., O. V. Melnichenko, P. P. Niiler, and H. Sasaki (2008), Stationary mesoscale jet-like features in the ocean, *Geophys. Res. Lett.*, *35*, L08603, doi:10.1029/2008GL033267.

Maximenko, N. A., P. Niiler, M.-H. Rio, O. Melnichenko, L. Centurioni, D. Chambers, V. Zlotnicki, and B. Galepin (2009), Mean dynamic topography of the ocean derived from satellite and drifting buoy data using three different techniques, *J. Atmos. Oceanic Technol.*, *26*, 1910–1919, doi:10.1175/2009JTECHO672.1.

Pavlis, N., S. A. Holmes, S. C. Kenyon, and J. K. Factor (2008), An Earth gravitational model to degree 2160: EGM2008, paper presented at General Assembly 2008, Eur. Geosci. Union, Vienna, 13–18 Apr.

Qiu, B., and S. Chen (2010), Eddy-mean flow interaction in the decadally modulating Kuroshio Extension system, *Deep Sea Res. Part II*, *57*, 1098–1110.

Rio, M.-H. (2010), Absolute dynamic topography from altimetry: Status and prospects in the upcoming GOCE era, in *Oceans From Space, Revisited*, edited by V. Barale, J. F. R. Gower, and L. Alberotanza, pp. 165–179, Springer, New York.

Rio, M.-H., and F. Hernandez (2003), High-frequency response of wind-driven currents measured by drifting buoys and altimetry over the world ocean, *J. Geophys. Res.*, *108*(C8), 3283, doi:10.1029/2002JC001655.

Rio, M.-H., and F. Hernandez (2004), A mean dynamic topography computed over the world ocean from altimetry, in-situ measurements and a geoid model, *J. Geophys. Res.*, *109*, C12032, doi:10.1029/2003JC002226.

Rio, M.-H., et al. (2005), The estimation of the ocean mean dynamic topography through the combination of altimetric data, in-situ measurements and GRACE geoid: From global to regional studies, paper presented at GOCINA International Workshop, Eur. Cent. for Geodyn. and Seismol., Luxembourg, 13–15 Apr.

Rio, M.-H., et al. (2007), A mean dynamic topography of the Mediterranean Sea computed from altimetric data, in-situ measurements and a general circulation model, *J. Mar. Syst.*, *65*, 484–508, doi:10.1016/j.jmarsys.2005.02.006.

Saraceno, M., C. Provost, and U. Zajaczkovski (2009), Long-term variation in the anticyclonic ocean circulation over the Zapiola Rise as observed by satellite altimetry: Evidence of possible collapses, *Deep Sea Res. Part I*, *56*, 1077–1092, doi:10.1016/j.dsr.2009.03.005.

Simmons, A., S. Uppala, D. Dee, and S. Kobayashi (2006), ERA-Interim: New ECMWF reanalysis products from 1989 onwards, in *ECMWF Newsl.*, *110*, 25–35.

Sudre, J., and R. A. Morrow (2008), Global surface currents: A high-resolution product for investigating ocean dynamics, *Ocean Dyn.*, *58*, 101–118, doi:10.1007/s10236-008-0134-9.

Tapley, B., D. Chambers, S. Bettadpur, and J. Ries (2003), Large scale ocean circulation from the GRACE GGM01 geoid, *Geophys. Res. Lett.*, *30*(22), 2163, doi:10.1029/2003GL018622.

Thompson, K. R., J. Huang, M. Véronneau, D. G. Wright, and Y. Lu (2009), Mean surface topography of the northwest Atlantic: Comparison of estimates based on satellite, terrestrial gravity, and oceanographic observations, *J. Geophys. Res.*, *114*, C07015, doi:10.1029/2008JC004859.

Vianna, M. L., and V. V. Menezes (2010), Mean mesoscale global ocean currents from geodetic pre-GOCE MDTs with a synthesis of the North Pacific circulation, *J. Geophys. Res.*, *115*, C02016, doi:10.1029/2009JC005494.

Vianna, M. L., V. V. Menezes, and D. P. Chambers (2007), A high resolution satellite-only GRACE-based mean dynamic topography of the South Atlantic Ocean, *Geophys. Res. Lett.*, *34*, L24604, doi:10.1029/2007GL031912.

Willis, J. K., J. M. Lyman, G. C. Johnson, and J. Gilson (2009), In situ data biases and recent ocean heat content variability, *J. Atmos. Oceanic Technol.*, *26*, 846–852, doi:10.1175/2008JTECHO608.1.

S. Guinehut, G. Larnicol, and M. H. Rio, CLS, DOS, 8-10 Rue Hermès, Parc Technologique du Canal, F-31520 Ramonville Saint-Agne, France. (mrio@cls.fr)